

The TESS-Keck Survey XXI: 13 New Planets and Homogeneous Properties for 21 Subgiant Systems

ASHLEY CHONTOS,^{1,2,*} DANIEL HUBER,^{1,3} SAMUEL K. GRUNBLATT,⁴ NICHOLAS SAUNDERS,¹ JOSHUA N. WINN,²
 MASON MCCORMACK,⁵ EMIL KNUDSTRUP,^{6,7} SIMON H. ALBRECHT,⁷ IAN J. M. CROSSFIELD,⁸ JOSEPH E. RODRIGUEZ,⁹
 DAVID R. CIARDI,¹⁰ KAREN A. COLLINS,¹¹ JON M. JENKINS,¹² ALLYSON BIERYLA,¹¹ NATALIE M. BATALHA,¹³ COREY BEARD,^{14,†}
 FEI DAI,^{15,16} PAUL A. DALBA,¹⁷ TARA FETHEROLF,^{18,19} STEVEN GIACALONE,^{16,‡} MICHELLE L. HILL,^{19,†} ANDREW W. HOWARD,¹⁶
 HOWARD ISAACSON,^{20,21} STEPHEN R. KANE,¹⁹ JACK LUBIN,^{22,23} MASON G. MACDOUGALL,²² TEO MOČNIK,²⁴
 JOSEPH M. AKANA MURPHY,^{17,§} ERIK A. PETIGURA,²² DARIA PIDHORODETSKA,¹⁹ ALEX S. POLANSKI,²⁵ PAUL ROBERTSON,¹⁴
 RYAN A. RUBENZAHL,^{16,§} EMMA V. TURTELBOOM,²⁶ LAUREN M. WEISS,²⁷ JUDAH VAN ZANDT,²² GEORGE R. RICKER,²⁸
 ROLAND VANDERSPEK,²⁸ DAVID W. LATHAM,¹¹ SARA SEAGER,^{28,29,30} SAMUEL N. QUINN,¹¹ AVI SHPORER,²⁸ NORA L. EISNER,^{31,¶}
 ROBERT F. GOEKE,²⁸ ALAN M. LEVINE,²⁸ ERIC B. TING,¹² STEVE HOWELL,¹² JOSHUA E. SCHLIEDER,³² PAUL BENNI,³³
 ANDREW W. BOYLE,¹⁶ TIANJUN GAN,³⁴ ERIC GIRARDIN,³⁵ ERICA GONZALEZ,³⁶ JOAO GREGORIO,³⁷ KEITH HORNE,³⁸
 JOHN LIVINGSTON,¹⁰ MICHAEL B. LUND,¹⁰ CHRISTOPHER R. MANN,³⁹ BOB MASSEY,⁴⁰ ELISABETH C. MATTHEWS,⁴¹
 KIM K. MCLEOD,⁴² ENRIC PALLE,^{43,44} ADAM POPOWICZ,⁴⁵ HOWARD M. RELLES,¹¹ RICHARD P. SCHWARZ,¹¹
 RAMOTHOLO SEFAKO,⁴⁶ GREGOR SRDOC,⁴⁷ THIAM-GUAN TAN,⁴⁸ GAVIN WANG,⁴⁹ CARL ZIEGLER,⁵⁰

¹Institute for Astronomy, University of Hawai'i, 2680 Woodlawn Drive, Honolulu, HI 96822, USA

²Department of Astrophysical Sciences, Princeton University, 4 Ivy Lane, Princeton, NJ 08544, USA

³Sydney Institute for Astronomy (SIfA), School of Physics, University of Sydney, NSW 2006, Australia

⁴Department of Physics and Astronomy, Johns Hopkins University, 3400 N Charles St, Baltimore, MD 21218, USA

⁵Department of Astronomy & Astrophysics, University of Chicago, Chicago, IL 60637, USA

⁶Department of Space, Earth and Environment, Chalmers University of Technology, 412 93, Gothenburg, Sweden

⁷Stellar Astrophysics Centre, Department of Physics and Astronomy, Aarhus University, Ny Munkegade 120, DK-8000 Aarhus C, Denmark

⁸Department of Physics & Astronomy, University of Kansas, 1082 Malott, 1251 Wescoe Hall Dr, Lawrence, KS 66045, USA

⁹Center for Data Intensive and Time Domain Astronomy, Department of Physics and Astronomy, Michigan State University, East Lansing, MI 48824, USA

¹⁰Caltech/IPAC-NASA Exoplanet Science Institute, 770 S. Wilson Avenue, Pasadena, CA 91106, USA

¹¹Center for Astrophysics | Harvard & Smithsonian, 60 Garden Street, Cambridge, MA 02138, USA

¹²NASA Ames Research Center, Moffett Field, CA 94035, USA

¹³Department of Astronomy and Astrophysics, University of California, Santa Cruz, CA 95060, USA

¹⁴Department of Physics & Astronomy, University of California Irvine, Irvine, CA 92697, USA

¹⁵Division of Geological and Planetary Sciences, 1200 E California Blvd, Pasadena, CA, 91125, USA

¹⁶Department of Astronomy, California Institute of Technology, Pasadena, CA 91125, USA^{**}

¹⁷Department of Astronomy and Astrophysics, University of California, Santa Cruz, CA 95064, USA

¹⁸Department of Physics, California State University, San Marcos, CA 92096, USA

¹⁹Department of Earth and Planetary Sciences, University of California, Riverside, CA 92521, USA

²⁰Department of Astronomy, University of California Berkeley, Berkeley CA 94720, USA

²¹Centre for Astrophysics, University of Southern Queensland, Toowoomba, QLD, Australia

²²Department of Physics & Astronomy, University of California Los Angeles, Los Angeles, CA 90095, USA

²³Department of Physics & Astronomy, The University of California Irvine, Irvine, CA 92697, USA

²⁴Gemini Observatory/NSF's NOIRLab, 670 N. A'ohoku Place, Hilo, HI 96720, USA

²⁵Department of Physics and Astronomy, University of Kansas, Lawrence, KS 66045, USA

²⁶Department of Astronomy, 501 Campbell Hall, University of California, Berkeley, CA 94720, USA

²⁷Department of Physics and Astronomy, University of Notre Dame, Notre Dame, IN 46556, USA

²⁸Department of Physics and Kavli Institute for Astrophysics and Space Research, Massachusetts Institute of Technology, 77 Massachusetts Avenue, Cambridge, MA 02139, USA

²⁹Department of Earth, Atmospheric and Planetary Sciences, Massachusetts Institute of Technology, 77 Massachusetts Avenue, Cambridge, MA 02139, USA

³⁰Department of Aeronautics and Astronautics, MIT, 77 Massachusetts Avenue, Cambridge, MA 02139, USA

³¹Center for Computational Astrophysics, Flatiron Institute, 162 Fifth Avenue, New York, NY 10010, USA

³²NASA Goddard Space Flight Center, 8800 Greenbelt Rd., Greenbelt MD, 22071, USA

³³Acton Sky Portal private observatory, Acton, MA, USA

³⁴Department of Astronomy, Tsinghua University, Beijing 100084, People's Republic of China

³⁵Grand-Pra Observatory, 1984 Les Hauderes, Switzerland

³⁶University of California, Santa Cruz, 1156 High Street, Santa Cruz, CA 95065, USA

³⁷Crow Observatory, Portalegre, Portugal

³⁸SUPA Physics and Astronomy, University of St. Andrews, Fife, KY16 9SS Scotland, UK

³⁹National Research Council Canada, Herzberg Astronomy & Astrophysics Research Centre, 5071 West Saanich Road, Victoria, BC V9E 2E7, Canada

⁴⁰Villa '39 Observatory, Landers, CA 92285, USA

⁴¹Max-Planck-Institut für Astronomie, Königstuhl 17, 69117 Heidelberg, Germany

⁴²Department of Astronomy, Wellesley College, Wellesley, MA 02481, USA

⁴³Instituto de Astrofísica de Canarias (IAC), 38205 La Laguna, Tenerife, Spain

⁴⁴Departamento de Astrofísica, Universidad de La Laguna (ULL), 38206, La Laguna, Tenerife, Spain

⁴⁵Silesian University of Technology, Department of Electronics, Electrical Engineering and Microelectronics, Akademicka 16, 44-100 Gliwice, Poland

⁴⁶South African Astronomical Observatory, P.O. Box 9, Observatory, Cape Town 7935, South Africa

⁴⁷Kotizarovci Observatory, Sarsoni 90, 51216 Viskovo, Croatia

⁴⁸Perth Exoplanet Survey Telescope, Perth, Western Australia

⁴⁹Tsinghua International School, Beijing 100084, China

⁵⁰Department of Physics, Engineering and Astronomy, Stephen F. Austin State University, TX 75962, USA

Abstract

We present a dedicated transit and radial velocity survey of planets orbiting subgiant stars observed by the TESS Mission. Using \sim 16 nights on Keck/HIRES, we confirm and characterize 12 new transiting planets – TOI-329 b, HD 39688 b (TOI-480), TOI-603 b, TOI-1199 b, TOI-1294 b, TOI-1439 b, TOI-1605 b, TOI-1828 b, HD 148193 b (TOI-1836), TOI-1885 b, HD 83342 b (TOI-1898), TOI-2019 b – and provide updated properties for 9 previously confirmed TESS subgiant systems (TOI-197, TOI-954, TOI-1181, TOI-1296, TOI-1298, TOI-1601, TOI-1736, TOI-1842, TOI-2145). We also report the discovery of an outer, non-transiting planet, TOI-1294 c ($P = 160.1 \pm 2.5$ d, $M_p = 148.3^{+18.2}_{-16.4} M_{\oplus}$), and three additional stars with long-term RV trends. We find that at least $19 \pm 8\%$ of subgiants in our sample of 21 stars have outer companions, comparable to main-sequence stars. We perform a homogeneous analysis of the stars and planets in the sample, with median uncertainties of 3%, 8% and 15% for planet radii, masses and ages, doubling the number of known planets orbiting subgiant stars with bulk densities measured to better than 10%. We observe a dearth of giant planets around evolved stars with short orbital periods, consistent with tidal dissipation theories that predict the rapid inspiral of planets as their host stars leave the main sequence. We note the possible evidence for two distinct classes of hot Jupiter populations, indicating multiple formation channels to explain the observed distributions around evolved stars. Finally, continued RV monitoring of planets in this sample will provide a more comprehensive understanding of demographics for evolved planetary systems.

1. INTRODUCTION

The existence of exoplanets orbiting stars in advanced evolutionary stages such as helium-core burning red giants (Hon et al. 2023), white dwarfs (Vanderburg et al. 2020) and pulsars (Wolszczan & Frail 1992) suggests that planets are able to withstand extreme environments present at the latest stages of stellar evolution. Most known exoplanets will face a similar fate as their host stars eventually evolve off the main-sequence (Kane 2023), yet the planet populations around post-main-sequence stars remain poorly understood.

The subgiant branch is a rapid phase in stellar evolution, causing stars with small differences in mass and age to have significantly different temperatures and radii. Both temperature and radii can now be precisely measured for most exoplanet host stars by combining photometry, spectroscopy and Gaia parallaxes (e.g. Berger et al. 2018), allowing subgiants to be well characterized and thus used to explore post-main-sequence planet demographics. For example, precise planet densities (which require precise knowledge of stellar radii and masses) are important to infer both the bulk compositions and atmospheric properties of exoplanets (Batalha et al. 2019). Indeed, while the number of planets orbiting subgiants is relatively small (\sim 15%), they are statistically overrepresented (\sim 32%) when only considering planets with the most precisely measured densities.

Precise ages are valuable for placing observational constraints on the timescales of important processes affecting

* Henry Norris Russell Fellow

† NASA FINESST Fellow

‡ NSF Astronomy and Astrophysics Postdoctoral Fellow

§ NSF Graduate Research Fellow

¶ Flatiron Research Fellow

** NASA Sagan Fellow

Table 1. TESS Subgiant Planet Sample

System	TOI	RA [$^{\circ}$]	Dec [$^{\circ}$]	V_{mag}	T_{mag}
New TESS systems					
TOI-329	329	351.32	-15.63	11.3	10.7
HD 39688	480	88.38	-16.27	7.3	6.8
TOI-603	603	141.11	+5.77	10.3	9.7
TOI-1199	1199	166.88	+61.35	11.1	10.4
TOI-1294	1294	223.09	+70.48	11.3	10.9
TOI-1439	1439	241.76	+67.88	10.6	10.0
TOI-1605	1605	54.48	+33.08	10.2	9.6
TOI-1828	1828	241.56	+69.62	11.6	11.1
HD 148193	1836	245.91	+54.69	9.8	9.3
TOI-1885	1885	304.67	+66.16	12.7	12.0
HD 83342	1898	144.56	+23.55	7.9	7.4
TOI-2019	2019	234.43	+48.96	10.3	9.6
Updated TESS systems					
HD 221416	197	353.03	-21.80	8.2	7.4
TOI-954	954	61.94	-25.21	10.3	9.8
TOI-1181	1181	297.22	+64.35	10.6	10.1
TOI-1296	1296	256.77	+70.24	11.4	10.8
TOI-1298	1298	241.32	+70.19	11.9	11.0
TOI-1601	1601	38.36	+41.01	10.7	10.1
TOI-1736	1736	43.44	+69.10	8.9	8.3
TOI-1842	1842	201.96	+9.03	9.8	9.3
TOI-2145	2145	263.76	+40.70	9.1	8.6

exoplanets. Previous studies suggested that the timescales for processes like tidal circularization and inward migration through tidal dissipation are strongly dependent on the orbital distance and stellar radius (Zahn 1977; Hut 1981; Zahn 1989). As the stellar radius rapidly changes for subgiant stars, stellar evolution is expected to affect tidal circularization timescales of close-in giant planets, producing a transient population of mildly eccentric planets orbiting evolved stars (Villaver & Livio 2009). *Kepler* and K2 data have yielded intriguing evidence which supports this theory, but were based on a small sample of planets (Van Eylen et al. 2016; Grunblatt et al. 2018; Chontos et al. 2019; Vissapragada et al. 2022).

Early radial velocity (RV) surveys aimed to probe the sensitivity of gas-giant planet occurrence to stellar mass using subgiant host stars (Johnson et al. 2007; Bowler et al. 2010; Johnson et al. 2013; Wolthoff et al. 2022). Additionally, *Kepler* and TESS have identified individual planets that transit subgiants for which masses could be measured (Chontos et al. 2019; Huber et al. 2019; Addison et al. 2021; Rodriguez et al. 2021; Saunders et al. 2022; Grunblatt et al.

2022, 2023). However, a systematic transit and radial velocity survey of subgiants has not yet been performed. In this paper we present a homogeneous population of TESS planets orbiting subgiant stars acquired as part of the TESS-Keck Survey (TKS; Chontos et al. 2022). Further RV monitoring of planets in this sample will provide a more comprehensive understanding of planet demographics for evolved systems.

2. SURVEY DESCRIPTION

2.1. Initial Target List

In order to select the most promising targets in a programmatic way, we assembled a master target list starting with the catalog of TESS Objects of Interest (TOI; Guerrero et al. 2021) and combined it with additional resources. The summary statistics for the TESS planet candidates were downloaded from the publicly-available database¹.

We queried the TESS Input Catalog (version 8, TICv8; Stassun et al. 2019) for stellar properties (e.g., radius, etc.) and available photometry (i.e. Johnson V and 2-MASS JHK) for the current list of TOIs, as well as corresponding *Gaia* (Gaia Collaboration et al. 2016, 2018) source IDs. The source IDs were then used to gather additional astrometric (i.e. RUWE) and photometric information from *Gaia* that were not directly accessible via TICv8. The California Planet Search (CPS) RV archive² was queried for targets since many of the bright TESS stars already have archival HIRES data available. As a final query, TOI dispositions were updated with the TESS Follow-up Observing Program (TFOP) Working Group³ (WG) Sub Group 1 (hereafter referred to as SG1).

The evolutionary state of the star was determined with evolstate⁴, given its effective temperature and surface gravity (Huber et al. 2017; Berger et al. 2018). Here, stellar parameters were first drawn from HIRES-derived spectroscopic parameters and then TICv8 if those were not available. In the event that parameters were not available from either of these sources, the parameters provided in the original TOI table were used.

2.2. Target Selection

When the survey was initially constructed, the maximum TOI number available was TOI-2145. From these candidates, we first removed TOIs with unfavorable or ambiguous SG1 dispositions (i.e. APC, BEB, FA, FP, NEB, PNEB, EB, SB1,

¹ <https://tev.mit.edu/>

² <https://jump.caltech.edu/>

³ <https://tess.mit.edu/followup/>

⁴ <https://github.com/danxhuber/evolstate/>

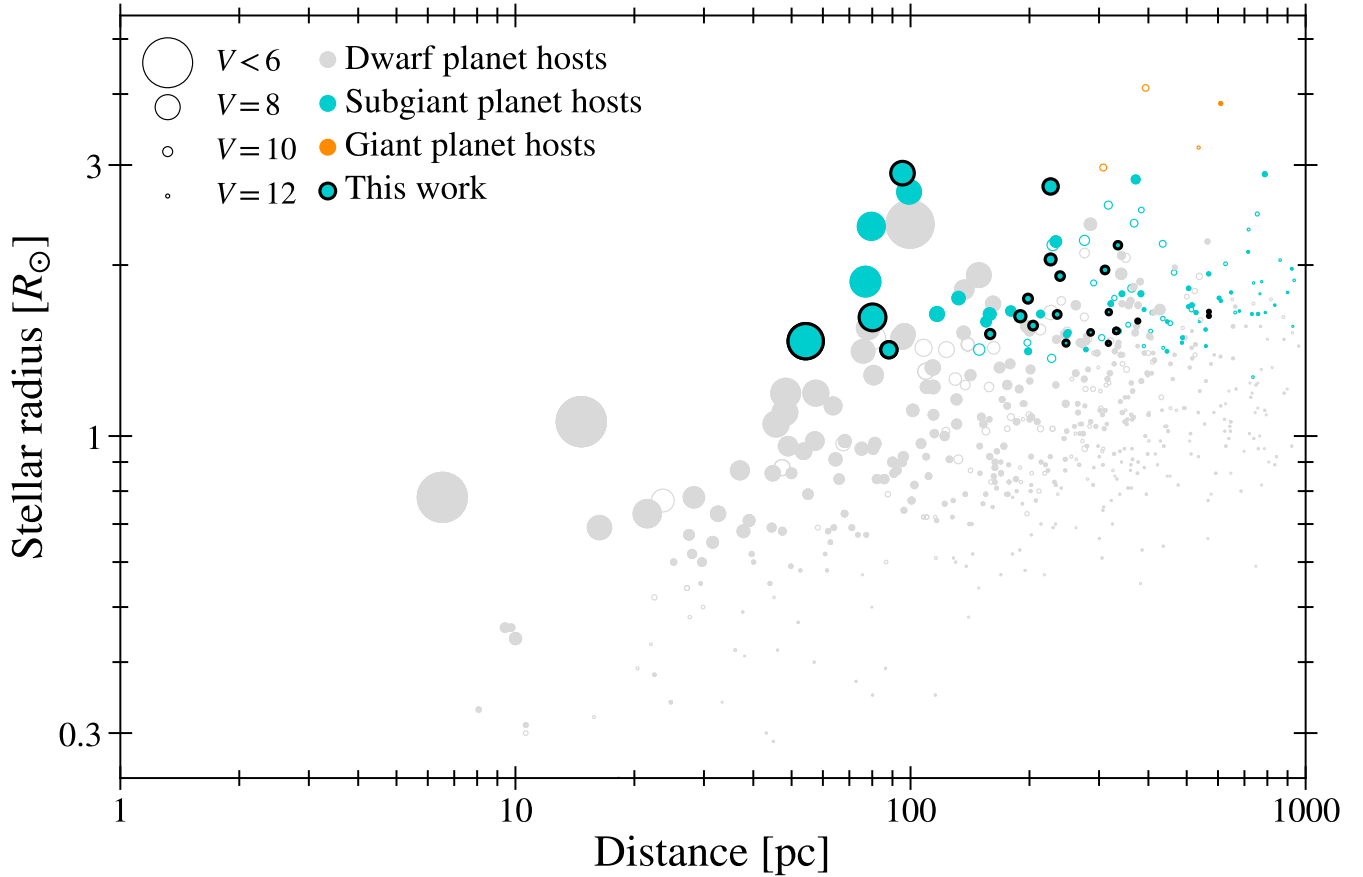


Figure 1. Stellar size and distance for stars that host exoplanets with measured densities according to the NASA Exoplanet Archive^b, colored by their approximate evolutionary state (i.e. Section 2.1). Markers are inversely sized by their visual magnitudes (i.e. bigger is brighter) and filled in for stars that host planets with the most precise ($\geq 4\sigma$) planet densities. The subgiant hosts in the present sample (highlighted with a thick, black outline) are, on average, closer and brighter than other known subgiant planet hosts.

^a <https://exoplanetarchive.ipac.caltech.edu>

^b <https://exoplanetarchive.ipac.caltech.edu>

SB2)⁵. False positive and unfavorable dispositions accounted for $\sim 25\%$ of the sample (514 TOIs). We excluded targets at low declinations ($\delta < -40^\circ$) that would not be accessible with Keck and also targets with a high *Gaia* re-normalized unit weight error⁶ (RUWE > 2), indicative of an unresolved companion (Belokurov et al. 2020; Evans 2018).

Finally, we performed a search for close companions for the remaining targets using their *Gaia* DR2 coordinates and the MAST (Mikulski Archive for Space Telescopes) Portal⁷. Any target with a relatively close ($< 2''$), bright ($\Delta V < 5$) companion or any companion within $1''$ were not considered for further follow-up, because of the danger that high-

resolution spectroscopy would be compromised by flux contamination from the secondary star during sub-optimal observing conditions. The final cut required a subgiant (SG) evolutionary state and brought the final sample down to 93 TOIs.

2.3. Target Vetting

Before being followed up with precise radial velocity (PRV) observations, the sample was subjected to one final round of vetting. The vetting described here was originally adapted from the TESS-Keck Survey (TKS) target selection work presented in Chontos et al. (2022) and is briefly summarized here.

Data validation (DV) reports from the SPOC (Science Processing Operations Center; Jenkins et al. 2016; Twicken et al. 2018; Li et al. 2019) and QLP (Quick Look Pipeline; Huang et al. 2020a,b) pipelines were downloaded and inspected. Careful consideration was given to standard diagnostics for threshold crossing events that indicate possible false positive

⁵ Ambiguous planet candidate (APC), blended eclipsing binary (BEB), false alarm (FA), false positive (FP), nearby eclipsing binary (NEB), probable nearby eclipsing binary (PNEB), eclipsing binary (EB), single-lined spectroscopic binary (SB1), double-lined spectroscopic binary (SB2)

⁶ <https://gea.esac.esa.int/archive/>

⁷ <https://mast.stsci.edu/portal/Mashup/Clients/Mast/Portal.html>

scenarios such as significant odd-even differences or large centroid offsets. Full DV reports were downloaded to examine the best-fit model and model parameters to identify any possible inconsistencies or other concerning features.

After passing the photometric vetting, targets were queued for reconnaissance (or recon) spectra to check for spectroscopic false positives (FP). All recon spectra were processed by ReaMatch (Kolbl et al. 2015) to search for and identify faint stellar companions in double-lined spectroscopic binaries. Systemic radial velocities, computed according to Chubak et al. (2012), were compared to those from *Gaia* to identify any large discrepancies which are indicative of single-lined spectroscopic binaries (SB1). Targets for which the recon and *Gaia* RV differed by more than 5 km s^{-1} typically failed this vetting step. However for more ambiguous cases near this cutoff, a second recon spectrum was taken to test for significant linear trends which provide additional evidence of the SB1-like nature.

2.4. Final Survey Sample

Our survey goal was to maximize the number of precise mass and density measurements of evolved TESS planets that could be obtained within the given 16-night Keck/HIRES allocation. Thus brighter targets and targets with existing HIRES data, both which would require less telescope time to achieve this goal, were typically prioritized to be vetted and followed up first. The final sample is provided in Table 1, which consists of 21 subgiant stars that have at least one transiting TESS planet candidates.

Figures 1 and 2 contextualize the sample with the current population of single stars that host planets with measured bulk densities. As expected with TESS, the stars in this sample are on average closer and brighter than other subgiant stars known to be transiting planet hosts. The stars in the sample also span a wide range of masses and ages, as expected for subgiant stars.

3. OBSERVATIONS

3.1. TESS Photometry

We downloaded all available light curve products for each target by using the MAST⁸ Portal, which primarily came from the SPOC and QLP pipelines. In order to decide which light curves would be used in the joint transit and RV analysis (Section 5.3), we inspected all available light curve data to look for systematics or other undesirable features as a result of differences in data reduction methods. Table 2 summarizes the TESS data that was available for the sample during the analysis, including how many sectors a given target was

Table 2. Number of sectors of available TESS data

System	TOI	20s	120s	600s	1800s
HD 221416	197	1	2*	1	1
TOI-329	329	–	2*	2	1
HD 39688	480	–	2*	1	1
TOI-603	603	1	4*	3	1
TOI-954	954	–	1*	1	2
TOI-1181	1181	–	19*	10	12
TOI-1199	1199	–	2*	2	2
TOI-1294	1294	–	5*	5	6
TOI-1296	1296	5	18*	8	12
TOI-1298	1298	–	19*	10	13
TOI-1439	1439	–	19*	10	13
TOI-1601	1601	–	–	–	1*
TOI-1605	1605	1	1	–	1*
TOI-1736	1736	3	6*	1	3
TOI-1828	1828	–	20*	10	13
HD 148193	1836	1	7*	4	4
TOI-1842	1842	–	2*	1	1
TOI-1885	1885	–	10*	3	8
HD 83342	1898	–	4*	3	1
TOI-2019	2019	–	3*	1	3
TOI-2145	2145	–	4*	3	2

*Indicates the data used for the joint fits (Section 5.3).

observed for, at which cadence(s) and which data was used for further analyses.

For the planet fits we typically used the specially curated TESS light curves, corresponding to the PDC-SAP (pre-search data conditioning; Smith et al. 2012; Stumpe et al. 2012, 2014) flux from the SPOC pipeline and the KSP-SAP (for *Kepler* spline) flux from the QLP pipeline. Light curves were then processed following the methodology in Chontos et al. (2019). To summarize, light curve processing included rejecting points with poor quality flags, clipping outliers by using a sliding two-day filter at the 5σ level, and flattening out-of-transit data by applying a median boxcar filter. As a final step, only data within ± 1.5 times the transit duration (centered on the mid-transit times) was retained to speed up the planet-fitting routine.

3.2. HIRES Radial Velocities

The survey results presented here were conducted over 16 nights in 2020 and 2021 using the High-Resolution Echelle Spectrometer (HIRES; Vogt et al. 1994), which is mounted on the 10-m Keck I telescope on Maunakea in Hawai‘i. Observations were acquired as part of the TESS-Keck Survey (TKS), where baselines for program targets are on average ~ 2 years. HIRES operates in the spectral range of

⁸ Mikulski Archive for Space Telescopes (MAST) <https://mast.stsci.edu/portal/Mashup/Clients/Mast/Portal.html>

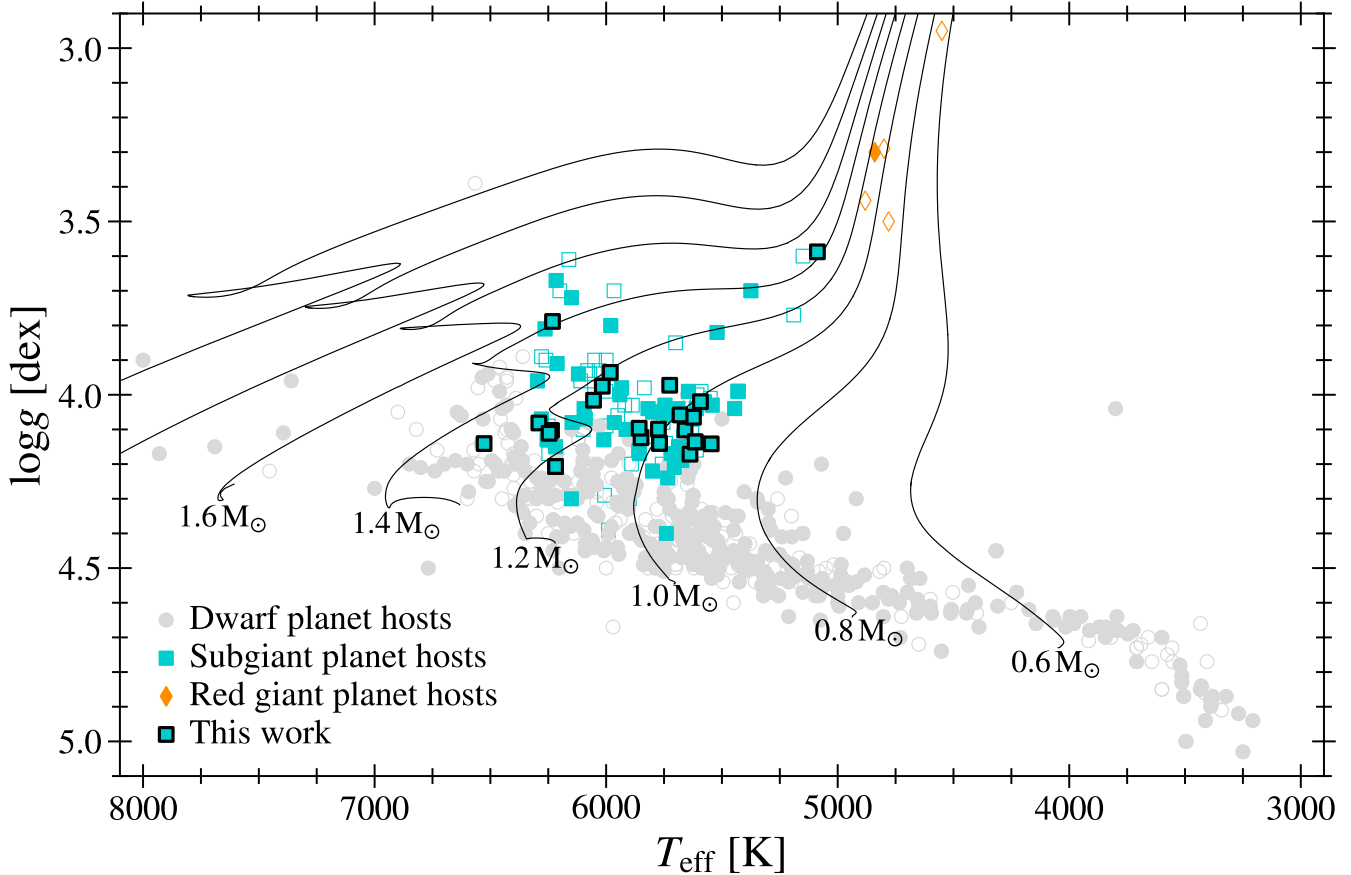


Figure 2. Same as Figure 1 but in a Kiel diagram, plotted with surface gravity and effective temperature. Here, markers also indicate stars of different evolutionary states. MIST solar-metallicity tracks are added for reference.

0.3 – 1.0 microns and uses an iodine cell configuration that when placed in the light path imprints a dense forest of absorption lines and thus serves as a robust wavelength calibration from which Doppler shifts can be measured (Butler et al. 1996).

Every target presented in this sample has two iodine-free observations: 1) a low S/N recon spectrum and 2) a high S/N template. A recon spectrum is an iodine-free exposure with an S/N of $\approx 40/\text{pixel}$ to check for false positives as part of the vetting procedure discussed in Section 2.3. A “template” is also an iodine-free exposure but typically obtained at a very high S/N, since this is used to compute the rest of the RVs for a given target. The rest of the iodine-in observations were reduced according to the well-tested procedures of the California Planet Search documented in Howard et al. (2010).

3.3. HARPS-N Radial Velocities

We acquired high-resolution ($R = 115000$) spectra of HD 148193 with the High Accuracy Radial velocity Planet Searcher for the Northern hemisphere (HARPS-N; Cosentino et al. 2012) mounted on the 3.58 m Telescopio Nazionale Galileo (TNG) located on Roque de los Muchachos, La

Palma, Spain. A total of 46 spectra were collected between UT 2021 February 13 and UT 2021 June 21. We set the exposure time to 900 s, which led to a median SNR of ~ 75 per pixel at 550 nm. We used the second fibre of the instrument to monitor the sky background. The HARPS-N spectra were reduced and extracted using the dedicated Data Reduction Software (DRS; Lovis & Pepe 2007) available at the telescope.

Ground-based RV observations for the sample are summarized in Table 3, including the number of observations per target, the first and last observation date and current baseline coverage. All radial velocity data used in the analysis are provided in Table 4.

3.4. High-resolution Imaging

Table 5 summarizes the high-resolution imaging observations acquired for targets that are being published for the first time. Our targets HD 39688 and TOIs 603, 1294, 1439, 1605, and 2019 were all observed using Keck/NIRC2 natural guide star adaptive optics imaging in the $2.2\mu\text{m}$ Brattet- γ (Br- γ) filter. We obtained the data in narrow-angle mode to provide a pixel scale of $\sim 0.01''$ and a total field of view of $\sim 10''$. We used NIRC2’s standard three-point, 3''-step dither pattern to

Table 3. Summary of RV observations taken of the sample. All RVs in this work are made publicly available in Table 4.

System	TOI	N RVs (unbinned)	Instrument	First Observation [UT]	Last Observation [UT]	Baseline [yr]
HD 221416	197	57 (64)	HIRES	2018 Nov 3	2021 Dec 25	3.1
TOI-329	329	43	HIRES	2020 Jun 3	2021 Dec 25	1.6
HD 39688	480	62 (181)	HIRES	2019 Dec 27	2021 Dec 26	2.0
HD 39688	480	20 (33)	HARPS-N	2019 Sep 26	2023 Feb 20	3.4
TOI-603	603	12	HIRES	2020 Oct 31	2022 May 13	1.5
TOI-954	954	28	HIRES	2020 Aug 27	2021 Nov 26	1.2
TOI-1181	1181	50 (87)	HIRES	2019 Dec 2	2022 May 16	2.5
TOI-1199	1199	16	HIRES	2019 Dec 10	2022 May 13	2.4
TOI-1294	1294	32	HIRES	2020 Mar 10	2022 May 13	2.2
TOI-1296	1296	24	HIRES	2019 Nov 28	2022 May 16	2.5
TOI-1298	1298	22	HIRES	2020 Jun 3	2022 May 13	1.9
TOI-1439	1439	53	HIRES	2020 Mar 10	2022 May 13	2.2
TOI-1601	1601	37	HIRES	2020 Feb 25	2022 Dec 31	1.8
TOI-1605	1605	44	HIRES	2020 Aug 26	2022 Sep 2	1.3
TOI-1736	1736	77 (79)	HIRES	2020 Aug 2	2022 Jan 19	2.0
TOI-1736	1736	35 (37)	HARPS-N	2020 Oct 10	2023 Feb 20	2.3
TOI-1828	1828	19	HIRES	2020 Jun 12	2022 May 13	1.9
HD 148193	1836	53	HIRES	2020 May 26	2022 May 13	2.0
HD 148193	1836	45	HARPS-N	2021 Feb 13	2021 Jul 21	0.5
TOI-1842	1842	38	HIRES	2020 May 26	2022 May 9	1.2
TOI-1885	1885	15	HIRES	2020 Jun 10	2022 May 13	1.9
HD 83342	1898	48	HIRES	2020 Jun 10	2022 May 13	2.1
TOI-2019	2019	43	HIRES	2020 Jun 24	2022 May 13	1.9
TOI-2145	2145	40	HIRES	2020 Aug 25	2022 May 13	1.7

Table 4. All radial velocities used in this work.

System	Time [BJD]	RV [ms ⁻¹]	RV Unc. [ms ⁻¹]	Instrument
...
TOI-329	2459028.108213	-9.74	2.15	HIRES
...

(This table is available in machine-readable form.)

avoid the noisy, lower-left detector quadrant. We acquired three sets of dithers for each target, with 0.5 positional offsets between each observation. Data were analyzed following Furlan et al. (2017).

No companions were detected for our sample, with the exception of TOI-1836, which was observed using the PHARO (Palomar High Angular Resolution Observer) instrument on the 5-m Hale telescope at the Palomar Observatory in California. The observations of TOI-1836 were taken on (UT) 2021-06-22 with the narrowband Br- γ filter. The sensitivity curve and image preview is shown in Figure 3, revealing a companion at a separation of $\rho = 0.819''$ with $\Delta m = 5.722$. The zoomed out image on the right of Figure 3 shows a 0.2''

binary (TIC 207468069) approximately 10'' away that is astrometrically associated with TOI-1836. We include the analysis and results from the joint fits discussed in Section 5.3 but later remove TOI-1836 b from the discussion in Section 7.

4. HOST STAR CHARACTERIZATION

4.1. High-resolution Spectroscopy

Spectroscopic stellar parameters ([Fe/H], T_{eff} , $v \sin i$, $\log g$) were derived using SpecMatch. SpecMatch derives parameters either from synthetic model atmospheres (i.e. SpecMatch-Synth; Petigura 2015) or empirically from a library of HIRES templates (i.e. SpecMatch-Emp; Yee et al. 2017), the latter of which was primarily developed for later-type cool dwarfs.

Initial inspections of recon spectra for the sample reported effective temperatures in the range $5080 \text{ K} < T_{\text{eff}} < 6600 \text{ K}$. Therefore, we adopted the derived spectroscopic values from SpecMatch-Synth for the entire sample. These values are subjected to uncertainties of $\sigma_{T_{\text{eff}}} = 100 \text{ K}$ in effective temperature, $\sigma_{\log g} = 0.1 \text{ dex}$ in surface gravity, $\sigma_{[\text{Fe}/\text{H}]} = 0.06 \text{ dex}$ in metallicity, and $\sigma_{v \sin i} = 1.0 \text{ km s}^{-1}$ in projected velocity.

Table 5. Summary of high-resolution imaging observations (Section 3.4) for new TESS systems presented in this work.

System	Instrument	Observation Date [UT]	Filter	Resolution [FWHM]	Contrast at 0. ^{''} 5 [Δ mag]
TOI-329	Palomar/PHARO	2019 Jul 13	Br- γ	0. ^{''} 10	7.0
HD 39688	Keck/NIRC2	2019 Mar 25	K-cont	0. ^{''} 05	8.4
TOI-603	Keck/NIRC2	2019 Jun 09	K-cont	0. ^{''} 05	7.5
TOI-1199	Palomar/PHARO	2020 Jan 08	Br- γ	0. ^{''} 13	6.2
TOI-1294	Keck/NIRC2	2020 May 28	K-cont	0. ^{''} 05	7.9
TOI-1439	Keck/NIRC2	2020 May 28	Br- γ	0. ^{''} 05	7.9
TOI-1605	Keck/NIRC2	2020 Sep 09	Br- γ	0. ^{''} 05	6.8
TOI-1605	Keck/NIRC2	2020 Sep 09	J-cont	0. ^{''} 03	6.9
HD 148193	Palomar/PHARO	2021 June 22	Br- γ	0. ^{''} 09	6.8
HD 148193	Palomar/PHARO	2021 June 22	H-cont	0. ^{''} 08	7.8
HD 83342	Palomar/PHARO	2020 Dec 04	Br- γ	0. ^{''} 14	6.1
TOI-2019	Keck/NIRC2	2020 Sep 09	K _s	0. ^{''} 05	7.3

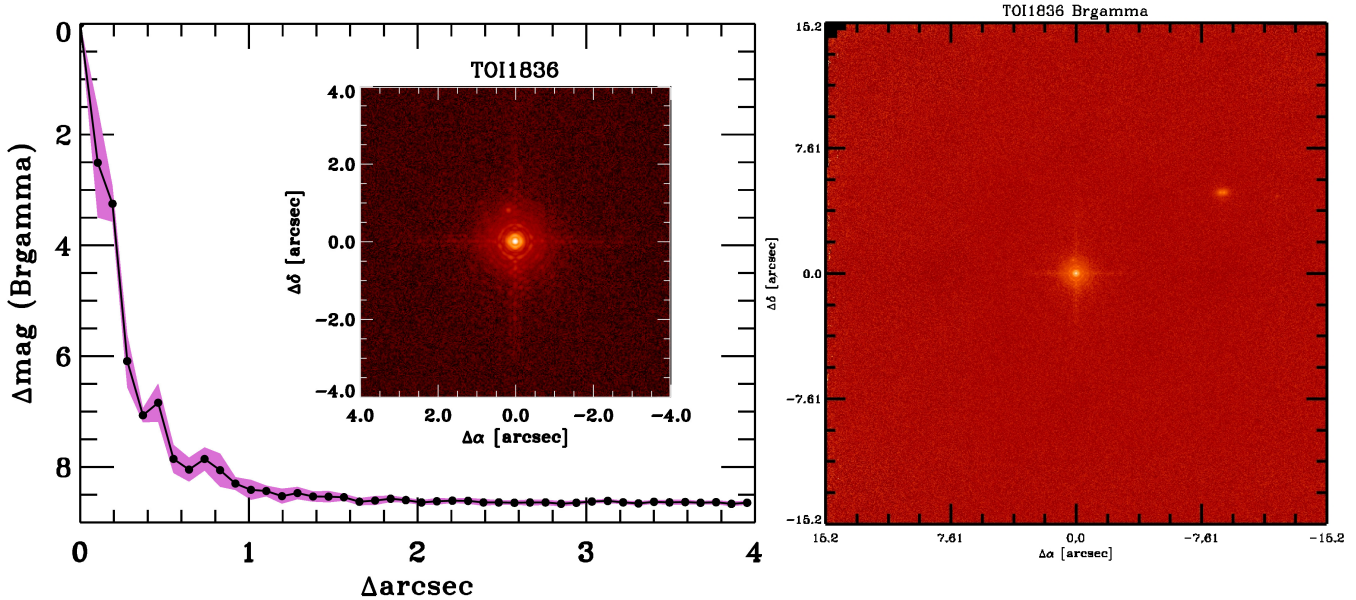


Figure 3. High-resolution image of TOI-1836 taken by the PHARO instrument at Palomar on UT 2021-06-22 in the narrowband Br- γ filter. Imaging revealed a multiple star system in an interesting hierarchy, the primary star which is orbited by a single star in addition to a well-separated binary at a projected separation of 10''.

4.2. Broadband Photometry and Gaia Parallax

We derived fundamental stellar properties from MIST (MESA Isochrones and Stellar Tracks; Choi et al. 2016) model grids, as implemented in `isoclassify`⁹ (Huber et al. 2017). Given a set of observables (i.e., photometry, spectroscopy, etc.), `isoclassify` interpolates the stellar grids to derive properties like their masses, luminosities, radii, densities and ages.

We used the values of T_{eff} and [Fe/H] (discussed in the previous section) as spectroscopic inputs, along with parallaxes from Gaia Data Release 3 (DR3; Gaia Collaboration et al. 2021, 2023). In order to further constrain the results and fit for extinction directly, we also included Johnson BV photometry, JHK_s from 2MASS (Skrutskie et al. 2006) and GB_pR_p from Gaia (Gaia Collaboration et al. 2021, 2023). For Gaia DR3 photometry, we adopted a systematic noise floor of 0.01 mag. A summary of derived stellar parameters are provided in Table 6. We note that the uncertainties on the reported masses, radii, densities and ages are intrinsic preci-

⁹ <https://github.com/danxhuber/isoclassify>

Table 6. Summary of subgiant host star properties

TOI	TIC	Spectroscopy*				$R_\star [R_\odot]$	Derived parameters†		
		$T_{\text{eff}} [\text{K}]$	$\log g [\text{cgs}]$	[Fe/H]	$v \sin i$		$M_\star [M_\odot]$	$\bar{\rho}_\star [\text{g cm}^{-3}]$	Age [Gyr]
197	441462736	5080 ± 90	3.584 ± 0.010	-0.08 ± 0.08	<2.0	2.943 ± 0.064	1.212 ± 0.074	0.067 ± 0.001	4.9 ± 1.1
329	169765334	5635	4.00	+0.18	<2.0	$1.52^{+0.04}_{-0.04}$	$1.07^{+0.06}_{-0.04}$	0.300 ± 0.034	$8.3^{+1.4}_{-2.0}$
480	317548889	6224	4.23	+0.17	8.7	$1.49^{+0.05}_{-0.03}$	$1.28^{+0.03}_{-0.03}$	0.385 ± 0.032	$2.6^{+0.6}_{-0.6}$
603	262746281	5894	4.07	+0.20	4.0	$1.58^{+0.03}_{-0.03}$	$1.23^{+0.04}_{-0.07}$	0.309 ± 0.020	$4.2^{+1.6}_{-0.7}$
954	44792534	5788	3.85	+0.40	3.4	$1.90^{+0.04}_{-0.04}$	$1.37^{+0.03}_{-0.11}$	0.196 ± 0.015	$3.4^{+1.6}_{-0.4}$
1181	229510866	6107	4.02	+0.42	10.6	$1.93^{+0.04}_{-0.04}$	$1.47^{+0.03}_{-0.03}$	0.204 ± 0.014	$2.2^{+0.3}_{-0.3}$
1199	99869022	5619	3.92	+0.42	<2.0	$1.46^{+0.03}_{-0.03}$	$1.15^{+0.05}_{-0.06}$	0.366 ± 0.028	$6.2^{+2.0}_{-1.4}$
1294	219015370	5690	4.02	+0.27	<2.0	$1.55^{+0.03}_{-0.03}$	$1.16^{+0.07}_{-0.06}$	0.310 ± 0.025	$6.1^{+1.9}_{-1.5}$
1296	219854185	5562	3.88	+0.42	<2.0	$1.68^{+0.04}_{-0.03}$	$1.16^{+0.12}_{-0.04}$	0.241 ± 0.033	$6.9^{+1.1}_{-2.4}$
1298	237104103	5783	4.01	+0.41	2.6	$1.45^{+0.03}_{-0.03}$	$1.21^{+0.03}_{-0.06}$	0.395 ± 0.032	$4.3^{+1.8}_{-0.8}$
1439	232982558	5843	4.02	+0.22	2.6	$1.61^{+0.03}_{-0.03}$	$1.23^{+0.04}_{-0.09}$	0.291 ± 0.024	$4.5^{+1.8}_{-0.8}$
1601	139375960	6020	3.94	+0.36	5.7	$2.20^{+0.06}_{-0.07}$	$1.51^{+0.04}_{-0.05}$	0.140 ± 0.013	$2.3^{+0.4}_{-0.3}$
1605	101037590	5752	4.06	+0.00	<2.0	$1.49^{+0.03}_{-0.03}$	$1.04^{+0.05}_{-0.04}$	0.308 ± 0.030	$8.3^{+1.4}_{-1.4}$
1736	408618999	5724	4.21	+0.16	<2.0	$1.41^{+0.03}_{-0.03}$	$1.08^{+0.06}_{-0.05}$	0.382 ± 0.033	$7.3^{+1.8}_{-1.9}$
1828	232982938	5780	4.04	+0.14	<2.0	$1.56^{+0.03}_{-0.03}$	$1.17^{+0.06}_{-0.07}$	0.302 ± 0.023	$5.5^{+1.8}_{-1.3}$
1836	207468071	6198	4.18	-0.13	5.9	$1.66^{+0.03}_{-0.03}$	$1.22^{+0.03}_{-0.08}$	0.265 ± 0.018	$3.5^{+1.3}_{-0.5}$
1842	404505029	6084	3.98	+0.33	6.2	$2.02^{+0.04}_{-0.04}$	$1.47^{+0.03}_{-0.04}$	0.175 ± 0.013	$2.4^{+0.4}_{-0.3}$
1885	258510872	6617	4.31	+0.03	7.8	$1.62^{+0.04}_{-0.04}$	$1.19^{+0.05}_{-0.08}$	0.272 ± 0.024	$3.7^{+1.4}_{-0.6}$
1898	91987762	6241	4.18	-0.10	7.0	$1.62^{+0.03}_{-0.03}$	$1.23^{+0.03}_{-0.06}$	0.283 ± 0.021	$3.4^{+1.0}_{-0.5}$
2019	159781361	5630	3.89	+0.41	1.6	$1.73^{+0.03}_{-0.03}$	$1.20^{+0.11}_{-0.04}$	0.233 ± 0.024	$6.0^{+1.0}_{-2.0}$
2145	88992642	6232	4.00	+0.29	17.8	$2.69^{+0.06}_{-0.06}$	$1.78^{+0.04}_{-0.05}$	0.091 ± 0.006	$1.2^{+0.1}_{-0.1}$

NOTE—

Values for TOI-197 were adopted from the asteroseismic analysis in Huber et al. (2019).

* Spectroscopic parameters were derived with SpecMatch-Synth (Petigura et al. 2017a) (see Section 4.1), which has the following systematic uncertainties: $\sigma_{T_{\text{eff}}} = 100$ K in effective temperature; $\sigma_{\log g} = 0.1$ dex in surface gravity; $\sigma_{[\text{Fe}/\text{H}]} = 0.06$ dex in metallicity; $\sigma_{v \sin i} = 1.0$ km s $^{-1}$ in projected velocity.

† Derived stellar parameters were estimated from model grids using isoclassify (Huber et al. 2017). Reported uncertainties are intrinsic precisions of the sample. When comparing these values to other methods, systematic errors as described in Tayar et al. (2022) should be considered.

sions of the sample. When comparing these values to other methods, systematic errors as described in Tayar et al. (2022) should be considered.

5. PLANET CHARACTERIZATION

5.1. System Confirmation

We fitted Keplerian orbits to all systems with significant RV variations that are in phase with reported transits seen by TESS. Keplerian RV orbits are described by the orbital period (P), argument of periastron (ω), orbital eccentricity (e), Doppler velocity semi-amplitude (K) as well as the time of inferior conjunction (T_{conj}). We also included instrument-specific “jitter” (σ) and RV offset (γ) terms. RV models can be further described by long-term properties which include linear ($\dot{\gamma}$) and quadratic ($\ddot{\gamma}$) acceleration terms, referred to as trend and curvature respectively. The two parameters $\dot{\gamma}$ and $\ddot{\gamma}$ capture additional Keplerian signals present in a time se-

ries with periods longer than the timespan of the available data. We did not fit for curvature in any system and linear trends were only added in systems that required an additional parameter to reasonably fit the data, the latter which is discussed in more detail in the following section.

Each system was fit with a single-planet model using radvel (Fulton et al. 2018), which performs rigorous model fitting and selection using well-known metrics (i.e. BIC, AIC, etc.). Since transits typically constrain periods well, we placed strong Gaussian priors on the periods using the values and uncertainties reported by TESS. For conjunction times we placed flat, uniform priors and enforced positive Doppler semi-amplitudes ($K > 0$). Finally, to avoid implicit biases we used the default radvel fitting basis $\{P, T_{\text{conj}}, \sqrt{e} \cos \omega, \sqrt{e} \sin \omega, K\}$.

For a given iteration, the system was initialized with all available parameters and then radvel iterated through all

Table 7. Models used during joint transit and RV fits (Section 5.3).

System	TOI	Model
HD 221416	197	1-planet model
TOI-329	329	1-planet model
HD 39688	480	1-planet model
TOI-603	603	1-planet model
TOI-954	954	1-planet model
TOI-1181	1181	1-planet model
TOI-1199	1199	1-planet model
TOI-1294	1294	2-planet model + linear trend
TOI-1296	1296	1-planet model
TOI-1298	1298	1-planet model
TOI-1439	1439	1-planet model
TOI-1601	1601	1-planet model
TOI-1605	1605	1-planet model + linear trend
TOI-1736	1736	2-planet model + linear trend
TOI-1828	1828	1-planet model + linear trend
HD 148193	1836	1-planet model
TOI-1842	1842	1-planet model
TOI-1885	1885	1-planet model
HD 83342	1898	1-planet model
TOI-2019	2019	1-planet model
TOI-2145	2145	1-planet model

combinations of free parameters. In other words, we set the initial number of possible parameters, which in the case of a single planet here is at most eight (i.e. P_b , K_b , e_b , ω_b , T_{conj_b} , σ_i , γ_i , $\dot{\gamma}$). Each system required several iterations of this procedure in order to identify the best possible solution and ultimately, confirm that we were recovering the same signal identified by TESS.

5.2. Searching for Additional Companions

With continued RV follow up, some systems exhibited significant scatter that could not be explained by a single-planet model alone. Since it has been shown that RV data can be systematically contaminated by stellar variability (Lubin et al. 2021), we first estimated what the expected contribution would be from the host star given its physical properties. This step was especially important with our sample of evolved host stars, which are notoriously more noisy than their main-sequence counterparts. We calculated the stellar “jitter” using Equation 3 from Chontos et al. (2022), which includes noise contributions from granulation and p-mode oscillations (Yu et al. 2018), as well as rotation (Chontos et al. 2022) and activity (Isaacson & Fischer 2010). We then use four categories to understand their long-term characteristics:

1. Systems with observations that behaved as expected (observed scatter \approx expected scatter). This included many of the known TESS systems in Figure 4, including HD 221416, TOI-954, TOI-1296, TOI-1298, TOI-1601, and TOI-1842. TOI-603, a new confirmation, also falls into this category but has a limited number of RVs.
2. Systems that show evidence for additional companions through significant linear trends. Figure 6 shows 3 newly confirmed TESS systems, TOI-1294 (left), TOI-1605 (middle) and TOI-1828 (right), all which showed significant RV offsets between observing seasons that could only be explained by an additional companion. The other system is TOI-1736, which also exhibits an astrometric acceleration and therefore, may be affected by a distant but bound stellar companion. For the systems that included a linear trend component, time references were defined as the midpoint of the RV time series and are included in the supplementary table(s).
3. Systems with scatter higher than expected due to the presence of new non-transiting companions detected in the RV observations. Here, we define “non-transiting” as a planet with no reported detection of a transit in the TESS photometry. For systems in this category, we implemented a blind search approach by adding parameters for a second planet to the model, whose only constraint was the orbital period, which was restricted to one half of the total observation baseline. To facilitate the interpretation of various models, the analysis was complemented by `rvsearch`¹⁰, which is a tool to search for Keplerian signals in RV time series data (Rosenthal et al. 2021). For example, we typically ranked a potential planet relatively high when `radvel` converged on a fairly precise period which was then matched by a significant period peak in the `rvsearch` results. In other words, `rvsearch` was not used to enforce more strict priors but used as a second interpretation of the system. Our three new, non-transiting planetary detections are discussed in Section 6 in more detail.
4. Systems with higher residual RV scatter than expected but no straightforward model to best explain the current set of observations. For systems like TOI-1181, TOI-1885 and TOI-2145, residual scatter exceeded 50 m s^{-1} . The residuals were also high for TOI-329, TOI-1199, TOI-1439, HD 148193 (TOI-1836), HD 83342 (TOI-1898) and TOI-2019 but did not exceed 50 m s^{-1} . In none of these systems was there an

¹⁰ <https://github.com/California-Planet-Search/rvsearch>

Table 8. Priors used for the joint transit and RV fitting analysis discussed in Section 5.3.

Parameter	Symbol	Units	Prior
<i>Default model parameters</i>			
<i>Instrument-specific terms</i>			
TESS zero-point offset	z	ppm	$\mathcal{U}[-\infty; +\infty]$
Keck/HIRES RV offset	γ	m s^{-1}	$\mathcal{U}[-\infty; +\infty]$
<i>Transiting planet parameters</i>			
Mean stellar density	$\bar{\rho}_*$	g cm^{-3}	$\mathcal{U}[0; +\infty]$
Limb-darkening coefficient 1	u_1		$\mathcal{N}(x; 0.6)[0, 2]$
Limb-darkening coefficient 2	u_2		$\mathcal{N}(x; 0.6)[-1, 1]$
Orbital period	P	days	$\mathcal{U}[0; +\infty]$
Time of inferior conjunction	T_c	days	$\mathcal{U}[-\infty; +\infty]$
Impact parameter	b		$\mathcal{U}[0; 1 + R_p/R_*]$
Planet-to-star radius ratio	R_p/R_*		$\mathcal{U}[0; +\infty]$
Eccentricity	e		$1/e$
	$\sqrt{e} \sin \omega$		$\mathcal{U}[-1; 1]$
	$\sqrt{e} \cos \omega$		$\mathcal{U}[-1; 1]$
RV semiamplitude	K	m s^{-1}	$\mathcal{U}[0; +\infty]$
<i>Optional model parameters</i>			
<i>RV trends</i>			
Linear RV trend*	$\dot{\gamma}$	$\text{m s}^{-1} \text{d}^{-1}$	$\mathcal{U}[-\infty; +\infty]$
<i>Nontransiting planet parameters</i>			
Orbital period	P	days	$\mathcal{U}[0; 0.5 \times \text{baseline}]$
Time of inferior conjunction	T_c	days	$\mathcal{U}[-\infty; +\infty]$
Eccentricity	e		$1/e$
	$\sqrt{e} \sin \omega$		$\mathcal{U}[-1; 1]$
	$\sqrt{e} \cos \omega$		$\mathcal{U}[-1; 1]$
RV semiamplitude	K	m s^{-1}	$\mathcal{U}[0; +\infty]$

*Time reference was set to the RV baseline midpoint, which is provided in the tables for each system that included a trend.

obvious way to reduce the scatter with an additional companion and consequently, more RV observations are needed to reveal the true nature of the systems.

5.3. Joint Transit & RV Fitting

Table 7 defines the models used for each system. We simultaneously fit TESS photometry and RV data for each target, as indicated in Table 2 and Table 4, respectively. For fitting we followed Chontos et al. (2019), who used the `ktransit`¹¹ package, an implementation of the analytical model by Mandel & Agol (2002). The analysis uses the following parameters as model input: orbital period (P), mid-transit time (T_0), quadratic limb-darkening coefficients (u_1, u_2), mean stellar density ($\bar{\rho}_*$), impact parameter (b), ratio of the planet radius to the stellar radius (R_p/R_*) and Doppler amplitude (K_*). Other free parameters include the photometric (z) and spectroscopic (γ) zero-point offsets, the

eccentricity of the orbit as well as the argument of periastron, where e and ω are re-parameterized to avoid parameter biases.

Table 8 defines the standard priors assigned in the joint transit and RV fitting, which were generally flat, uninformative priors. We used weak priors for quadratic limb-darkening coefficients (LDCs) $\{u_1, u_2\}$ by setting Gaussian priors with wide widths ($\sigma = 0.6$) and centers set by theoretical TESS band values from Claret (2016), which are interpolated in T_{eff} , $\log g$ and $[\text{Fe}/\text{H}]$. Moreover, additional constraints on u_1 and u_2 were implemented to prevent the limb-darkening properties from taking nonphysical values (Burke et al. 2008; Barclay et al. 2015). We also implemented the $\{q_1, q_2\}$ parametrization from Kipping (2013) to more efficiently sample the two-dimensional LDC parameter space. We sampled uniformly in $e \cos \omega$ and $e \sin \omega$ and therefore also added an additional Jeffreys prior ($1/e$) to effectively set a uniform prior on eccentricity (Eastman et al. 2013).

¹¹ <https://github.com/mrtommyb/ktransit>

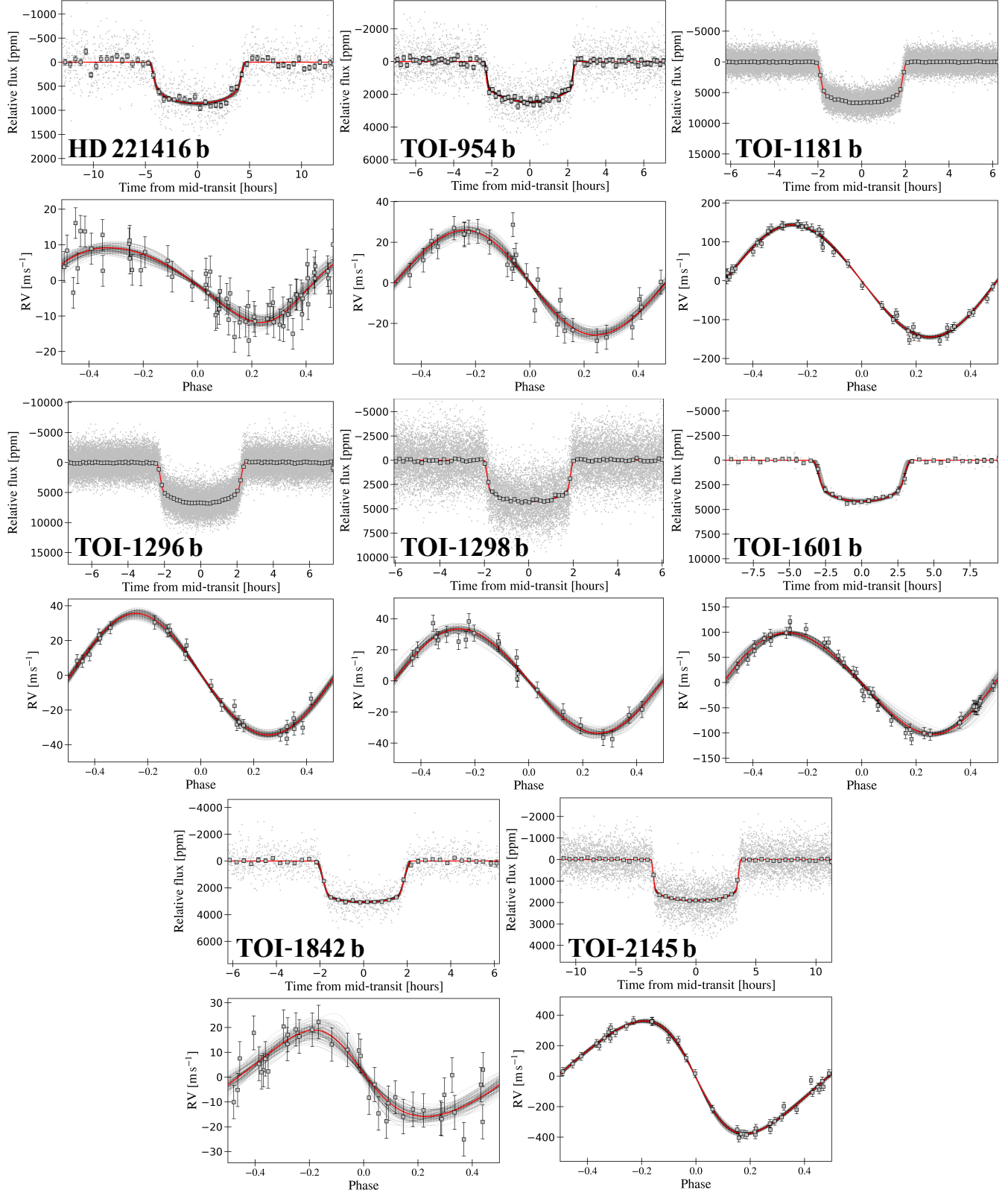


Figure 4. Phase-folded transit and radial velocity data for previously confirmed single-planet TESS systems: HD 221416 b (TOI-197; top left), TOI-954 b (top middle), TOI-1181 b (top right), TOI-1296 b (middle left), TOI-1298 b (middle middle), TOI-1601 b (middle right), TOI-1842 b (bottom left), and TOI-2145 b (bottom right). Best-fit joint models are overplotted in red, including 100 samples randomly drawn from posterior distributions and plotted in gray (with transparency) to show model uncertainties.

To sample the multi-dimensional parameter space, we used the affine-invariant ensemble Markov Chain Monte Carlo (MCMC) sampler, emcee (Foreman-Mackey et al. 2013). For joint global fits, we assumed a linear ephemeris and quadratic limb darkening law. Every joint transit and RV fit initialized 50 walkers, i.e., at least twice the maximum number of free parameters for a given system. Each walker took 10^4 steps and then implemented a burn-in phase of 10^3 steps before concatenating samples to obtain the final posterior distributions for the parameters.

Table 9 summarizes the primary properties of interest for the full subgiant planet sample, which uses HD designations where available and remaining targets are assigned by their TOI number. More than half are newly confirmed TESS systems, comprising TOI-329, HD 39688 (TOI-480), TOI-603, TOI-1199, TOI-1294, TOI-1439, TOI-1605, TOI-1828, HD 148193 (TOI-1836), TOI-1885, HD 83342 (TOI-1898) and TOI-2019. We also provide updated, homogeneous parameters for the 9 other known TESS systems in Table 1 (Huber et al. 2019; Rodriguez et al. 2021; Sha et al. 2021; Kabáth et al. 2022; Wittenmyer et al. 2022; Rodriguez et al. 2023; Akana Murphy et al. 2023).

5.4. Previously known TESS Systems

Our homogeneous sample of precise RVs combined with considerably longer time baselines than previous studies provides the opportunity to better characterize and understand evolved TESS systems. Figure 4 shows transit and RV data for previously confirmed systems plotted with our global results, as well as updated properties for each system in the supplementary tables. Here we summarize any major differences we find in the updated properties for known TESS systems.

Our most evolved system, HD 221416 (TOI-197), was the first asteroseismic host discovered by TESS and sits at the base of the red giant branch. Our derived mass of $M_p = 44.6 \pm 4.0 M_\oplus$ is nearly one third smaller than the value of $M_p = 60.5 \pm 5.7 M_\oplus$ reported in Huber et al. (2019), highlighting the importance for long-term RV monitoring. We also find a mild eccentricity ($e = 0.167 \pm 0.050$) that is consistent with their reported value of $e = 0.115 \pm 0.032$. Combining the eccentricity with the asteroseismic age, Huber et al. (2019) constrained the planetary tidal quality to be near or larger than a lower limit of $Q_p \approx 3.2 \times 10^4$, because otherwise the orbit would have already circularized within its lifetime of ~ 5 Gyr.

First identified by Sha et al. (2021), TOI-954 b is a short-period ($P = 3.68$ days) Saturn-sized planet. Sha et al. (2021) reported a value of $M_p = 55.3 \pm 5.6 M_\oplus$ while we found a mass that is 4σ higher ($M_p = 76.8 \pm 5.6 M_\oplus$). Our median eccentricity of $e = 0.045$ is smaller than the value of $e = 0.14$ reported by Sha et al. (2021), but both estimates are

consistent with zero. Finally, our 10σ mass measurement improves the bulk planet density precision by a factor of two, with $\bar{\rho}_p = 0.50^{+0.06}_{-0.05} \text{ g cm}^{-3}$.

Rodriguez et al. (2021) reported a bimodal posterior probability distributions for the mass and age of the TESS planet host TOI 1601, which they attributed to the star's relatively ambiguous location on an HR diagram given the precision of their observations. Our analysis agrees with their younger, more massive solution, with an age of 2.3 ± 0.4 Gyr and mass of $1.51 \pm 0.05 M_\star$.

6. NEW TESS SYSTEMS

Phase-folded data and global fits are shown for all new, single-planet TESS systems in Figure 5. New systems with significant RV trends, including TOI-1294, TOI-1605 and TOI-1828, are shown in Figure 6. We discuss each of the new TESS confirmations in the following subsections below. Planet properties derived from the global fits are summarized in Table 9.

6.1. TOI-329

The $V=11.3$ subgiant star is a cool ($T_{\text{eff}} = 5660 \pm 75$ K), low mass ($M_\star = 1.08 \pm 1.03 M_\odot$) star with a moderate metallicity of $[\text{Fe}/\text{H}] = +0.16 \pm 0.05$. The TOI-329.01 ~ 1 parts per thousand (ppt) transit-like events were also detected twice by TFOP SG1 ground-based transit observations in Sloan i' band using $7.8''$ photometric apertures that excluded the flux of all known Gaia DR3 stars. The SPOC difference image analysis for TOI-329.01 constrained the host star to within $1.2 \pm 3.3''$ of the location of the transit source.

Follow-up RV measurements resolved the 5.7 day orbit, where the phase-folded HIRES data in Figure 5 (top left) clearly demonstrate that the planet has a significantly ($\sim 13\sigma$) non-zero eccentricity. The planet is slightly larger than Neptune at $R_p \sim 4.7 R_\oplus$, which is a rare planet type in the context of the observed planet radius distribution (e.g., Fulton et al. 2017). We report a mass of $M_p = 40.8 \pm 3.6 M_\oplus$ and a bulk density of $\bar{\rho}_p = 2.13 \pm 0.54 \text{ g cm}^{-3}$. The combination of the relatively small separation ($a/R_\star \leq 10$) and older age (8.3 ± 1.0 Gyr) would suggest that the orbit has had sufficient time to circularize via tidal interactions of the planet with the host star. Yet the eccentricity is found to be moderate ($e = 0.39 \pm 0.03$), suggesting some other dynamical process as a potential source for the non-zero eccentricity.

6.2. HD 39688 (TOI-480)

TFOP SG1 ground-based lightcurves ruled out nearby eclipsing binaries as the source of the TOI-480.01 transit-like event detected in the TESS data. However, HD 39688 ($V=7.3$) is a challenging system since the host star has a rotational velocity of $\sim 8 \text{ km s}^{-1}$ while the estimated Doppler amplitude of the transiting $\sim 2.8 R_\oplus$ candidate was 2.8

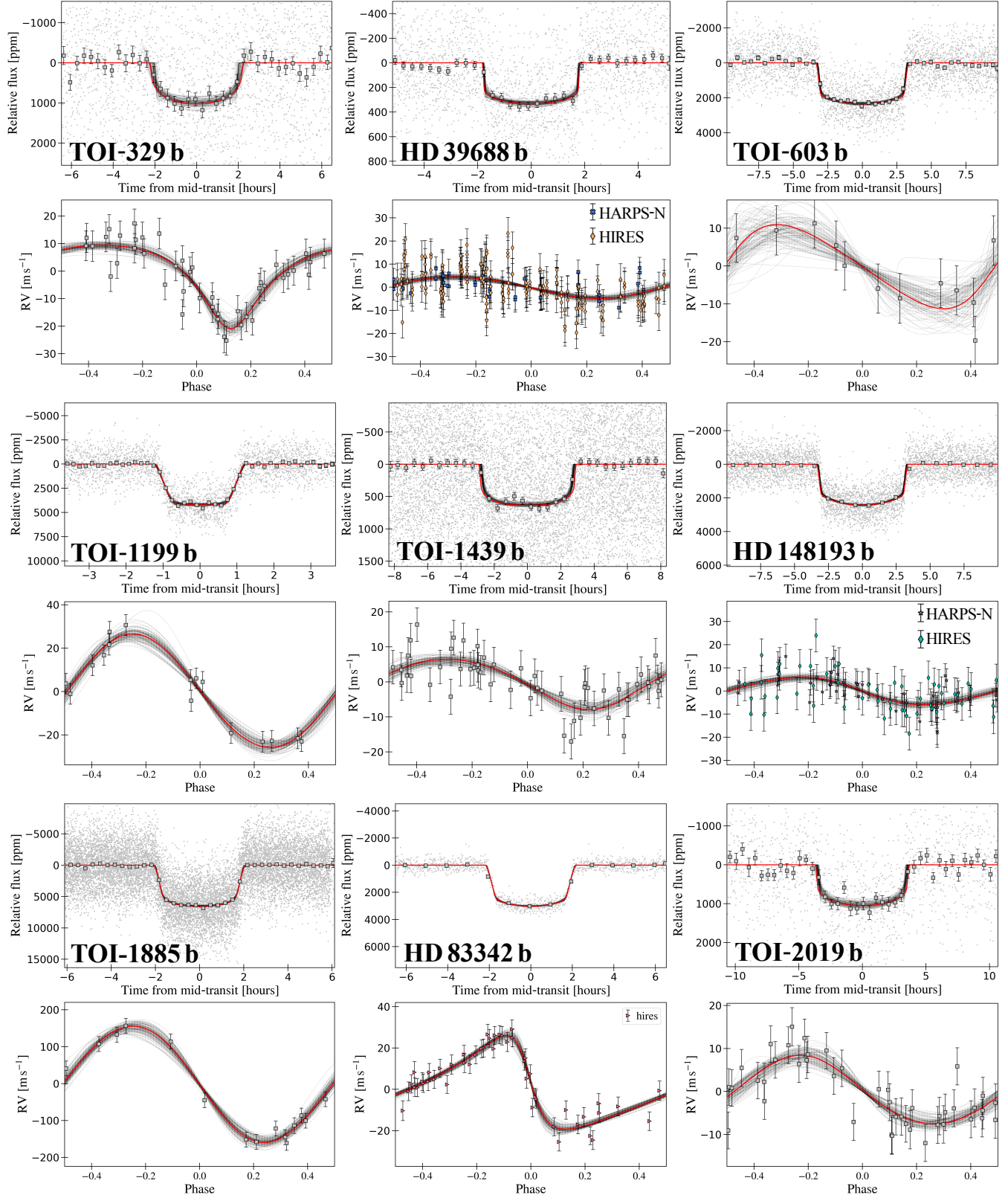


Figure 5. Same as Figure 4 but for new TESS single-planet systems: TOI-329 b (top left), HD 39688 b (TOI-480, top middle), TOI-603 b (top right), TOI-1199 b (middle left), TOI-1439 b (middle middle), HD 148193 b (TOI-1836; middle right), TOI-1885 b (bottom left), HD 83342 b (TOI-1898; bottom middle), and TOI-2019 (bottom right). Best-fit joint models are overplotted in red with 100 samples randomly drawn from posterior distributions and plotted in gray (with transparency) to demonstrate the model uncertainties.

m s^{-1} . The $\sigma_{\text{RV}} - v \sin i$ relation of Chontos et al. (2022) predicted an additional scatter of $\sim 2.6 \text{ m s}^{-1}$ in the time series due to the rotation. Therefore, during each visit to HD 39688 we obtained three back-to-back observations to improve the per-visit uncertainty by a factor of $\sqrt{3}$. The transit and RV observations indeed confirm the planetary nature of HD 39688 b ($M_p = 15.7 \pm 2.2 M_\oplus$), which has a bulk density consistent with a rocky, terrestrial planet ($\rho_p = 4.4 \pm 0.8 \text{ g cm}^{-3}$).

Due to the high $v \sin i$, we checked the raw TESS photometry (SAP-FLUX) for evidence of stellar rotation via star spot modulation. We identified a significant peak at a period of $P_{\text{rot}} \sim 6.92$ days, which if due to the host star rotation, suggests that the system is either near or at synchronous rotation with the transiting planet, which has an orbital period, $P \sim 6.86$ days. The stellar inclination to the line of sight measured from the observations (by combining $v \sin i$, P_{rot} , R_*) is $\sim 52^\circ$, which suggests a probable misalignment of the orbital plane of the planets with respect to the rotation axis of the star. In the event that the misalignment is confirmed then synchronization would not be expected.

6.3. TOI-603

The effective temperature and age of TOI-603 are roughly consistent with those of the Sun, with $T_{\text{eff}} = 5850 \pm 70 \text{ K}$ and an age of $4.9 \pm 1.2 \text{ Gyr}$. The subgiant star is larger and more massive though, with a size of $R_* = 1.56 \pm 0.03 R_\odot$ and a mass of $M_* = 1.20 \pm 0.05 M_\odot$. With only 12 HIRES RVs, the mass measurement of $M_p = 47.5 \pm 13.7 M_\oplus$ has the lowest statistical significance of all new confirmations, but the $\sim 3\sigma$ detection is sufficient to confirm the planetary nature of the transiting planet, TOI-603 b.

TOI-603.01 is one example from the TESS Primary Mission where an alias of the true period was reported; it was only observed for a single sector during the nominal mission, and it was initially assumed that a transit occurred during the data gap. Further TFOP efforts consistently confirmed that the period is close to twice that of the previously reported period, which is supported by the phase-folded HIRES RVs shown in Figure 5. Fortunately the target was re-observed in 2-minute cadence in the first Extended Mission in sectors 35, 45 and 46, which provided more transits to better constrain the observed planet properties (i.e. $R_p = 7.93 \pm 0.20 R_\oplus$, $P = 16.17989 \pm 0.00006$ days).

6.4. TOI-1199

TOI-1199 is one the smallest host stars in the sample, with $R_* = 1.46 \pm 0.02 R_\odot$, $T_{\text{eff}} = 5630 \pm 54 \text{ K}$ and an age of $\sim 6.3 \text{ Gyr}$. The transiting planet, TOI-1199 b, is a giant planet ($R_p = 10.6 \pm 0.3 R_\oplus$) on an approximately circular orbit with a period of $P \sim 3.7$ days. Using 16 HIRES RVs, we report a precise mass of $M_p = 69.4 \pm 5.7 M_\oplus$ and bulk density of $\bar{\rho}_p = 0.32 \pm 0.04 \text{ g cm}^{-3}$.

Intriguingly, a total of 7 different threshold crossing events (TCEs) with similar periods were all assigned to the same TIC, which we speculate is evidence for transit timing variations (TTVs). We also found additional power near the reported period in the residual RV periodogram after subtracting out the single-planet model, which could be evidence for another planet in the system. However given the small number of RVs, more observations are needed to confirm the existence of any additional companions.

6.5. TOI-1294

TOI-1294 is a massive ($M_* = 1.20 \pm 0.05 M_\odot$) and metal-rich ($[\text{Fe}/\text{H}] = +0.28 \pm 0.06$) host star, with an effective temperature of $T_{\text{eff}} \sim 5770 \pm 80 \text{ K}$ and age of $\sim 5.2^{+1.4}_{-0.9} \text{ Gyr}$. Achromatic ~ 3 ppt transit-like events were also detected on target by TFOP SG1 ground-based transit observations in Sloan g' and Sloan i' bands using $5.8''$ or smaller photometric apertures that excluded the flux of all known Gaia DR3 stars. Initial follow up RVs immediately confirmed the planetary nature of the transiting, Saturn-sized ($R_p = 9.2 \pm 0.3$) TOI-1294 b, with a mass of $M_p = 62.2 \pm 5.0 M_\oplus$ on a ~ 3.9 -day orbit.

A significant offset was observed during the second observing season near the 2400 time stamp, seen in the bottom left panel of Figure 6, which could only be explained by at least one additional companion. A blind RV search unambiguously recovered a Keplerian signal at a period of $P = 160.9 \pm 2.5$ days, with a mass corresponding to $M_p = 148.3 \pm 17.3 M_\oplus$, hereafter referred to as TOI-1294 c. The best-fit model also exhibits an RV trend of $\dot{\gamma} = 0.052 \pm 0.007 \text{ m s}^{-1} \text{ d}^{-1}$ ($T_{\text{ref}} = 2459198.114897$), where further RV observations will enable a more comprehensive understanding of the evolved, multi-planet TOI-1294 system.

6.6. TOI-1439

TOI-1439 ($V=10.6$) has an effective temperature $T_{\text{eff}} = 5857 \pm 60 \text{ K}$ and metallicity of $[\text{Fe}/\text{H}] = +0.22 \pm 0.06$. The radius and mass of the subgiant host are $R_* = 1.64 R_\odot$ and $M_* = 1.24 M_\odot$, respectively, and it has an intermediate age of $\sim 4.5^{+1.6}_{-0.6} \text{ Gyr}$. The observed activity indicator from the RV time series, $\log R'_{HK} = -5.26$, suggests that the star is relatively inactive. This is further supported by back-to-back HIRES observations obtained on UT 2020-07-27, which were separated by one hour and showed very little jitter.

TOI-1439 b is a Neptune-sized ($R_p = 4.1 \pm 0.2 R_\oplus$) planet on an orbit with a period of $P \sim 27.6$ days, which is slightly longer than a single TESS sector. We measured a mass and bulk density corresponding to $M_p = 38.4 \pm 5.5 M_\oplus$ and $\bar{\rho}_p = 2.9 \pm 0.6 \text{ g cm}^{-3}$, respectively. After subtracting the best-fit model from the RV time series, however, the residual RVs still showed high scatter and given the relatively inactive host

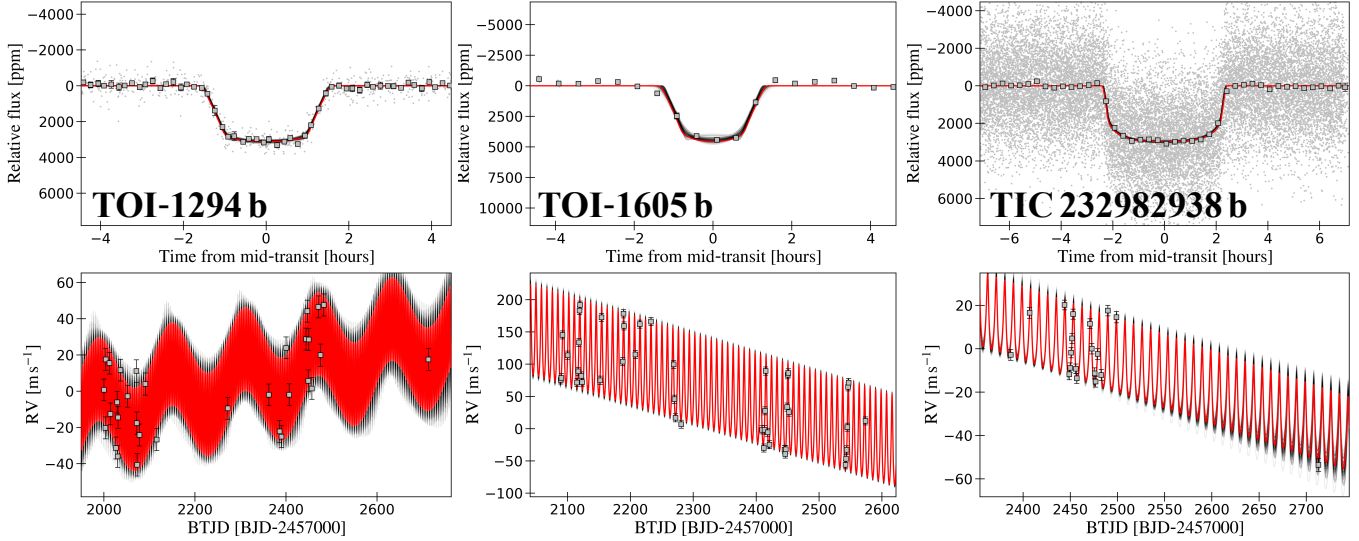


Figure 6. Phase-folded TESS photometry (top) and Keck/HIRES RV time series (bottom) with the joint transit and RV fit overplotted in red. The RV observations presented here enabled the discovery of non-transiting planetary companion, TOI-1294 c (Section 6.5), as well as three additional outer companions observed via significant trends in TOI-1294 (left), TOI-1605 (middle) and TOI-1828 (right).

star, could indicate the presence of additional planets in the system.

6.7. *TOI-1605*

TOI-1605 ($V=10.2$) has an effective temperature and metallicity which are fully consistent with those of the Sun, with $T_{\text{eff}} = 5774 \pm 75$ K and $[\text{Fe}/\text{H}] = +0.03 \pm 0.06$. The host star also has a radius of $R_{\star} = 1.51 \pm 0.03 R_{\odot}$, a mass of $M_{\star} = 1.05 \pm 0.03 M_{\odot}$, and an age of $\sim 7.9 \pm 1.0$ Gyr. Achromatic ~ 5 ppt transit-like events of TOI-1605.01 were detected by TFOP SG1 ground-based transit observations in multiple bands spanning Sloan g' through Pan-STARRS z -short bands.

TOI-1605 b is currently challenging to characterize, given the limited availability of TESS photometry and the high impact parameter that is implied by the v-shaped transit shown in Figure 6 (middle). The Jupiter-sized planet ($R_p = 10.34 \pm 0.64 R_{\oplus}$) has a mass of $M_p = 221.3 \pm 7.7 M_{\oplus}$ and is on an eccentric ($e = 0.28 \pm 0.01$) orbit, which is interesting given the short orbital period (< 10 days). As seen in the bottom of Figure 6, the RV observations also indicate the presence of an outer companion ($\dot{\gamma} = -0.298 \pm 0.006 \text{ m s}^{-1} \text{ d}^{-1}$ using a time reference of $T_{\text{ref}} = 2459497.065739$) that could be responsible for the observed high eccentricity but more RVs are needed to characterize the outer companion.

6.8. *TOI-1828*

The host star TOI-1828 ($V=11.6$) is a subgiant with an effective temperature of $T_{\text{eff}} = 5680$ K, a radius of $R_{\star} = 1.60 R_{\odot}$, and a mass of $M_{\star} = 1.06 M_{\odot}$. TFOP SG1 ground-based transit observations in Sloan g' and Sloan i' bands also detected achromatic ~ 3 ppt transit-like events of TOI-

1828.01 using $7.8''$ or smaller photometric apertures that excluded the flux of all known Gaia DR3 stars. The SPOC difference image analysis also constrained the host star to within $0.12 \pm 2.4''$ of the location of the transit source.

The close-in ($P = 9.094$ days), eccentric ($e = 0.31 \pm 0.03$) HJ is strikingly similar to TOI-1605 b (discussed above), with the exception of the lower planet mass of $M_p = 58.5 \pm 3.8$ (and bulk density of $\bar{\rho}_p = 0.50 \pm 0.05 \text{ g cm}^{-3}$). The panels on the right side in Figure 6 show the phase-folded TESS photometry (top) and RV time series (bottom). The last RV observation clearly indicates an additional companion in the system. As expected though, the single, most recent RV does not constrain the slope well but the measured trend is significant nevertheless, with $\dot{\gamma} = -0.147 \pm 0.012 \text{ m s}^{-1} \text{ d}^{-1}$ ($T_{\text{ref}} = 2459445.570399$).

6.9. *HD 148193 (TOI-1836)*

HD 148193 ($V=9.6$) is a young (~ 3.3 Gyr) and hot (~ 6235 K) star, and is one of the more metal-poor subgiants in the sample, with $[\text{Fe}/\text{H}] = -0.16$. As discussed in Section 3.4, HD 148193 is the only host star in the sample with any known stellar companions. High-resolution imaging revealed a close ($< 1''$, $\Delta m = 5.7$) companion and a $0.2''$ binary (TIC 207468069) that is $\sim 10''$ away. TFOP SG1 ground-based transit observations in Pan-STARRS z -short band and Cousins I band detected ~ 2.5 ppt transit-like events on target. The transiting ~ 20 -day planet HD 148193 b has a size of $R_p = 8.38 \pm 0.19 R_{\oplus}$ and a mass of $M_p = 28.4 \pm 4.3 M_{\oplus}$.

The SPOC pipeline more recently identified another candidate signal using data from the extended mission. The candidate is interior to the confirmed planet, with a radius of R_{\oplus}

Table 9. Summary of derived planet properties from the joint transit and RV fits.

Planet	P [days]	Epoch [BTJD]	R_p [R_\oplus]	M_p [M_\oplus]	$\bar{\rho}_p$ [g cm $^{-3}$]	e
HD 221416 b	14.2790 ± 0.0027	1357.0127 ± 0.0022	9.36 ± 0.33	44.6 ± 4.0	0.30 ± 0.04	0.17 ± 0.05
TOI-329 b	5.7044 ± 0.0001	2090.7935 ± 0.0049	4.72 ± 0.36	40.8 ± 3.6	2.13 ± 0.54	0.39 ± 0.03
HD 39688 b	6.86588 ± 0.00001	1469.5660 ± 0.0016	2.69 ± 0.10	15.7 ± 2.2	4.42 ± 0.80	0.10 ± 0.07
TOI-603 b	16.17989 ± 0.00006	2268.0635 ± 0.0015	7.93 ± 0.20	47.5 ± 13.7	0.52 ± 0.16	0.22 ± 0.19
TOI-954 b	3.6843 ± 0.0002	2145.2170 ± 0.0008	9.47 ± 0.25	76.8 ± 5.6	0.50 ± 0.06	0.05 ± 0.04
TOI-1181 b	2.1031937 ± 0.0000005	1957.8213 ± 0.0001	16.14 ± 0.34	374.7 ± 8.9	0.49 ± 0.03	0.01 ± 0.01
TOI-1199 b	3.67147 ± 0.00001	2611.4540 ± 0.0005	10.60 ± 0.33	69.4 ± 5.7	0.32 ± 0.04	0.05 ± 0.04
TOI-1294 b	3.91529 ± 0.00001	2393.0110 ± 0.0033	9.19 ± 0.31	62.2 ± 5.0	0.44 ± 0.06	0.07 ± 0.04
TOI-1294 c	160.1 ± 2.5	2349.0106 ± 5.7665	–	148.3 ± 17.0	–	0.10 ± 0.09
TOI-1296 b	3.944373 ± 0.000001	1930.7553 ± 0.0002	13.93 ± 0.30	95.4 ± 5.35	0.19 ± 0.02	0.02 ± 0.02
TOI-1298 b	4.537143 ± 0.000003	1929.5853 ± 0.0003	9.64 ± 0.21	98.3 ± 5.2	0.60 ± 0.05	0.03 ± 0.03
TOI-1439 b	27.643927 ± 0.000090	1703.4752 ± 0.0023	4.15 ± 0.18	38.4 ± 5.5	2.94 ± 0.57	0.15 ± 0.07
TOI-1601 b	5.33206 ± 0.00034	1793.2741 ± 0.0026	14.07 ± 0.49	361.4 ± 7.6	0.71 ± 0.08	0.07 ± 0.04
TOI-1605 b	8.7099 ± 0.0006	2887.4759 ± 0.0766	10.34 ± 0.64	221.3 ± 7.7	1.10 ± 0.21	0.28 ± 0.01
TOI-1736 b	7.073091 ± 0.000008	2740.5891 ± 0.0007	3.05 ± 0.19	11.9 ± 1.6	2.30 ± 0.50	0.04 ± 0.04
TOI-1736 c	571.3 ± 0.5	2273.1 ± 0.4	–	2477 ± 118	–	0.37 ± 0.01
TOI-1828 b	9.0941045 ± 0.0000083	1936.2770 ± 0.0007	8.62 ± 0.19	58.5 ± 3.8	0.50 ± 0.05	0.31 ± 0.03
HD 148193 b	20.38085 ± 0.000025	1933.1655 ± 0.0008	8.38 ± 0.19	28.4 ± 4.3	0.27 ± 0.04	0.14 ± 0.11
TOI-1842 b	9.573922 ± 0.000013	1933.3360 ± 0.0008	12.29 ± 0.32	73.4 ± 7.5	0.22 ± 0.03	0.18 ± 0.08
TOI-1885 b	6.544060 ± 0.000006	1958.2553 ± 0.0008	13.66 ± 0.41	516.4 ± 32.7	1.12 ± 0.12	0.04 ± 0.03
HD 83342 b	45.522149 ± 0.000039	1894.2540 ± 0.0005	9.74 ± 0.22	127.5 ± 6.6	0.76 ± 0.07	0.48 ± 0.04
TOI-2019 b	15.3444 ± 0.0055	1958.2895 ± 0.0040	5.66 ± 0.28	34.6 ± 4.2	1.05 ± 0.21	0.09 ± 0.07
TOI-2145 b	10.26111 ± 0.00001	2013.2807 ± 0.0006	12.25 ± 0.30	1810.2 ± 42.5	5.42 ± 0.42	0.21 ± 0.02

$= 2.5 R_\oplus$ and a period of $P = 1.77$ days, but ultimately its confirmation is beyond the scope of this paper.

6.10. TOI-1885

TOI-1885 is a young (2.0 ± 0.3 Gyr) and hot ($T_{\text{eff}} = 6527 \pm 98$ K) host star with a solar-like metallicity ([Fe/H] = $+0.02 \pm 0.05$). Gaia DR3 also reported an effective temperature that is fully consistent with the value of derived from the spectrum. The effective temperature of the star places it on the hot side of the Kraft break (Kraft 1967), suggesting that the host star lacks a significant convective envelope.

Our analysis estimates a planet size of $R_p = 13.66 \pm 0.41 R_\oplus$ and mass of $M_p = 516.4 \pm 32.7 M_\oplus$ ($\sim 1.6 M_J$), which together constrain the bulk density to $\sim 10\%$, with $\bar{\rho}_p = 1.12 \pm 0.12$ g cm $^{-3}$. The close-in giant planet has an orbital period of $P = 6.544$ days and appears to be on a nearly circular orbit, but more RVs could better constrain the eccentricity of the orbit.

6.11. HD 83342 (TOI-1898)

HD 83342 ($V=7.9$) was originally a community TESS object of interest due to the single transit that occurred during the nominal mission. However the target was reobserved for

two additional sectors in the extended mission, hence providing two additional transits to better constrain the orbital period of the transiting candidate TOI-1898.01. The planet HD 83342 b is a warm Jupiter ($P = 45.5$ days) with a mass of $M_p = 127.5 \pm 6.6 M_\oplus$ and is on a highly eccentric orbit with $e = 0.48 \pm 0.04$, as shown in the phase-folded RVs in the bottom left of Figure 5. The moderate $v \sin i$ of the host star also makes the system an ideal target to measure the sky-projected obliquity via Rossiter-McLaughlin or Doppler tomography observations, and especially because the highly eccentric, warm Jupiter could help elucidate gas giant formation and migration pathways.

6.12. TOI-2019

TOI-2019 is a cool (~ 5590 K), metal-rich ([Fe/H] = $+0.40 \pm 0.06$) star with an age of 6.7 ± 0.6 Gyr. Comparatively, the subgiant host has a more moderate size, with $R_\star = 1.75 \pm 0.03 R_\odot$ and a mass of $M_\star = 1.17 \pm 0.04 M_\odot$. The transiting planet, TOI-2019 b, is a rare planet type in context with the current distribution of planetary radii, with $R_p = 5.7 \pm 0.3 R_\oplus$, and is also one of the longer period planets in our sample, with $P = 15.35$ days. Our measured mass

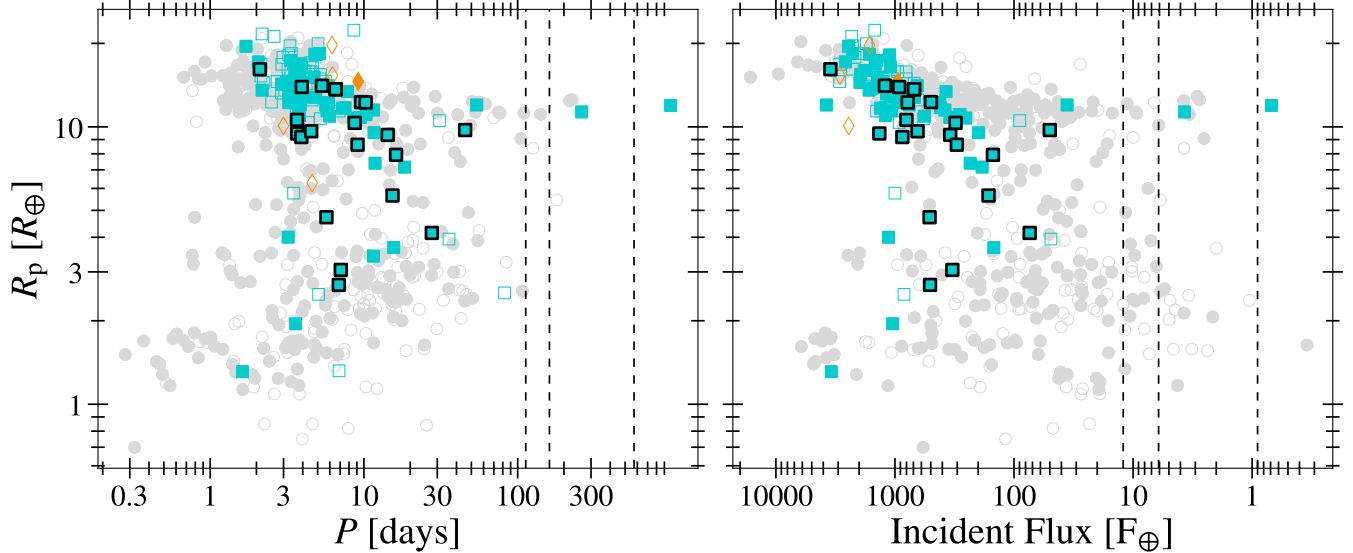


Figure 7. Planet size versus orbital period (left) and incident flux (right) for all planets with measured radii and masses. Evolutionary states of the host stars are indicated by different colors: main-sequence (grey), subgiants (cyan) and red giants (orange). Filled markers show planets with the most precise densities ($\geq 4\sigma$). Our subgiant sample is highlighted with thick black outlines, and positions for new non-transiting planets (i.e. with no measured sizes) are shown by vertical, dashed lines.

is $M_p = 34.60 \pm 4.26 M_\oplus$, which translates to a bulk planet density of $\bar{\rho}_p = 1.05 \pm 0.20 \text{ g cm}^{-3}$.

7. DISCUSSION

7.1. Planet Sizes and Multiplicity

Figure 7 shows planet sizes versus orbital period and incident flux for all planets with measured radii and masses, separated according to the evolutionary state of the host star. Literature values were taken from the NASA Exoplanet Archive¹². Our sample increases the number of known planets with measured radii and masses orbiting subgiant stars by 25%, bringing the total population to 106 planets. Further, our sample contribution increases to 50% when only considering planets with the most precisely measured ($\leq 10\%$) densities. Based on radius and incident flux, our sample consists mainly of warm and hot Jupiters and sub-Saturns, and a handful of sub-Neptune sized planets.

Figure 7 shows that planets orbiting subgiants show the same broad demographic features as planets orbiting main-sequence stars, including radius inflation with incident flux for gas-giant planets (Burrows et al. 2000; Lopez & Fortney 2016) and a dearth of planets with high-incident fluxes and radii between $\approx 3 - 8 R_\oplus$ (the sub-Neptune desert, Lundkvist et al. 2016). Quantitatively, planets orbiting subgiants are on average hotter and exclude the shortest orbital period planets. The former is consistent with selection bias, while the latter is consistent with tidal orbital period decay becom-

ing more efficient as a star evolves off the main-sequence, causing short period planets to be engulfed (Schlaufman & Winn 2013).

Our sample includes 4 subgiants with outer non-transiting companions. Sample targets have observations that span two years on average and therefore assuming each target has equal sensitivity to such companions, corresponds to an approximate occurrence rate of outer Jovian planets in subgiant systems of $19 \pm 8\%$. This fraction is consistent with the occurrence rate of Jovian planets beyond the ice line from long-term RV surveys (Fernandes et al. 2019; Fulton et al. 2021). Since subgiants are on average more massive than main-sequence stars, this may imply that the correlation of stellar mass and gas-giant planet occurrence does not extend to long orbital periods. We caution that the above numbers are not based on a detailed occurrence rate study (using injection/recovery tests), which is beyond the scope of this paper.

7.2. Mass-Radius Relation

Figure 8 compares the mass-radius relation and density versus radius for our sample with values for other planets drawn from the literature. For giant planets ($> 10 R_\oplus$) we observe that planets orbiting subgiant stars follow largely the same distribution as planets orbiting main-sequence stars. We observe a tentative lack of inflated, massive ($> 1000 M_\oplus$) planets around subgiant stars. However, a K-S test shows that this is not significant, likely due to the small sample size.

A large fraction of our newly confirmed planets fall in the region between Neptune and sub-Saturn sized planets, for which radii increase as $R_P \approx M_\oplus^{0.6}$, and Jovian planets,

¹² <https://exoplanetarchive.ipac.caltech.edu>

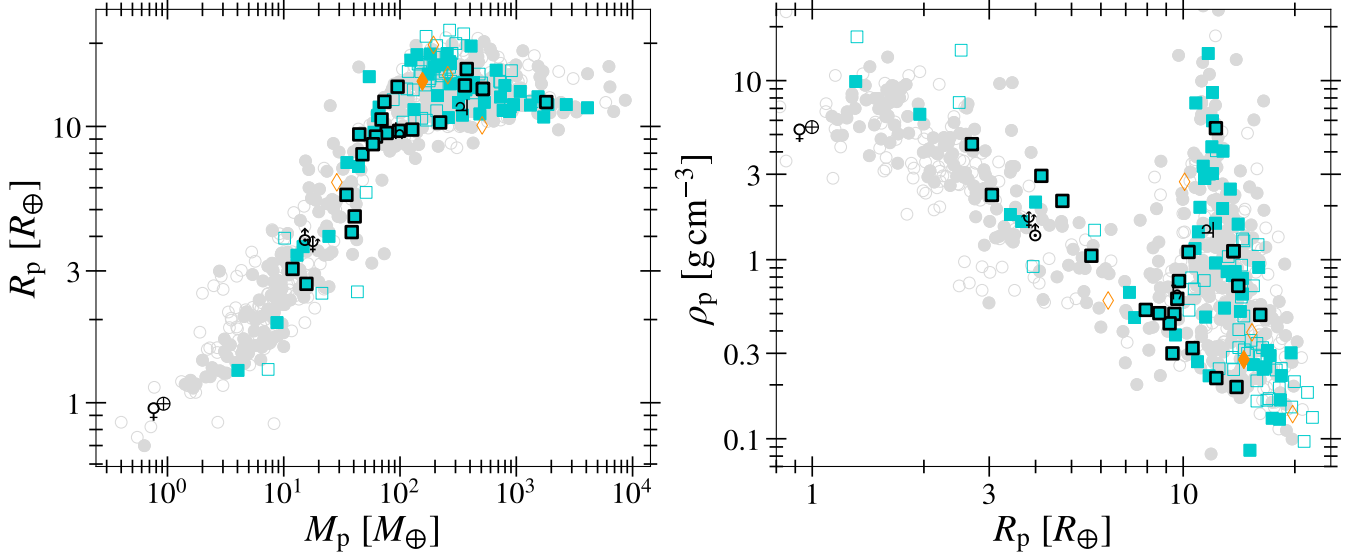


Figure 8. Same as Figure 7 but now showing planet radius versus planet mass (left) and bulk density versus planet radius (right). Solar system planets are shown by the black symbols.

for which radius is nearly constant with mass (Weiss et al. 2013; Chen & Kipping 2017). Sub-Saturn sized planets ($4\text{--}8 R_\oplus$) around main-sequence stars show a wide variety of masses, ($6\text{--}60 M_\oplus$), even at roughly fixed radius (Petigura et al. 2017b; Van Eylen et al. 2018). Conversely, our sample of planets orbiting subgiants appears to show a tighter mass range ($35\text{--}50 M_\oplus$), and the smallest ($< 4 R_\oplus$) planets found around subgiants are all consistently more massive. We speculate that this could signify that the atmospheres of low density planets are preferentially eroded away as the host star evolves into a subgiant. An alternative explanation is that low-mass planets are more difficult to confirm around subgiant stars, which exhibit increased RV jitter due to granulation.

7.3. Eccentricity and Age

Orbital eccentricities of exoplanets provide valuable clues for how planetary systems might have formed. For example, planet-planet scattering followed by high eccentricity migration is one of the favored formation scenarios for gas-giant planets on short orbits (Dawson & Johnson 2018). Our sample is particularly useful for investigations of such theories due to the precise age constraints for subgiant host stars. Indeed, recent studies have found that hot Jupiter occurrence decreases with stellar age (Hamer & Schlaufman 2019; Miyazaki & Masuda 2023; Chen et al. 2023).

Figure 9 shows orbital eccentricity versus age for all hot Jupiters ($R_p > 8 R_\oplus$, $P < 10$ days) in our sample. Intriguingly, some of the most eccentric planets in our sample are found orbiting around some of the oldest stars. This suggests that planet-planet scattering, which can lead to high eccentricities, may occur on $>$ Gyr timescales. Alternatively, it

suggests that tidal circularization can occur on significantly slower timescales than orbital period decay, consistent with a diversity of dissipation efficiencies.

Another clue for the dynamical architectures of these systems is the presence of outer, non-transiting companions. Figure 9 shows that planets without outer companions are preferentially young and on circular orbits. Conversely, planets with outer companions are preferentially older and on eccentric orbits. If confirmed, this would imply possible distinct formation pathways for different hot Jupiter populations in which some undergo high-eccentricity migration and circularize quickly, whereas those with outer companions possibly gain their eccentricities through Kozai-Lidov oscillations (Fabrycky & Tremaine 2007). Additional systems will be required to confirm the significance of this trend, given the small number statistics in this sample.

8. CONCLUSIONS

We presented a dedicated transit and radial velocity survey of planets orbiting subgiants observed by TESS. Our main conclusions can be summarized as follows:

- We measured radii and masses for the 23 planets orbiting 21 subgiant stars, 13 of which are new planet discoveries. Of the 21 transiting planets with measured sizes, 19 planets have bulk densities measured to better than 25%, including 6 with densities measured to better than 10%.
- Our sample includes 4 subgiants with outer non-transiting companions, corresponding to an approximate outer Jovian planet fraction of $19\pm8\%$. This frac-

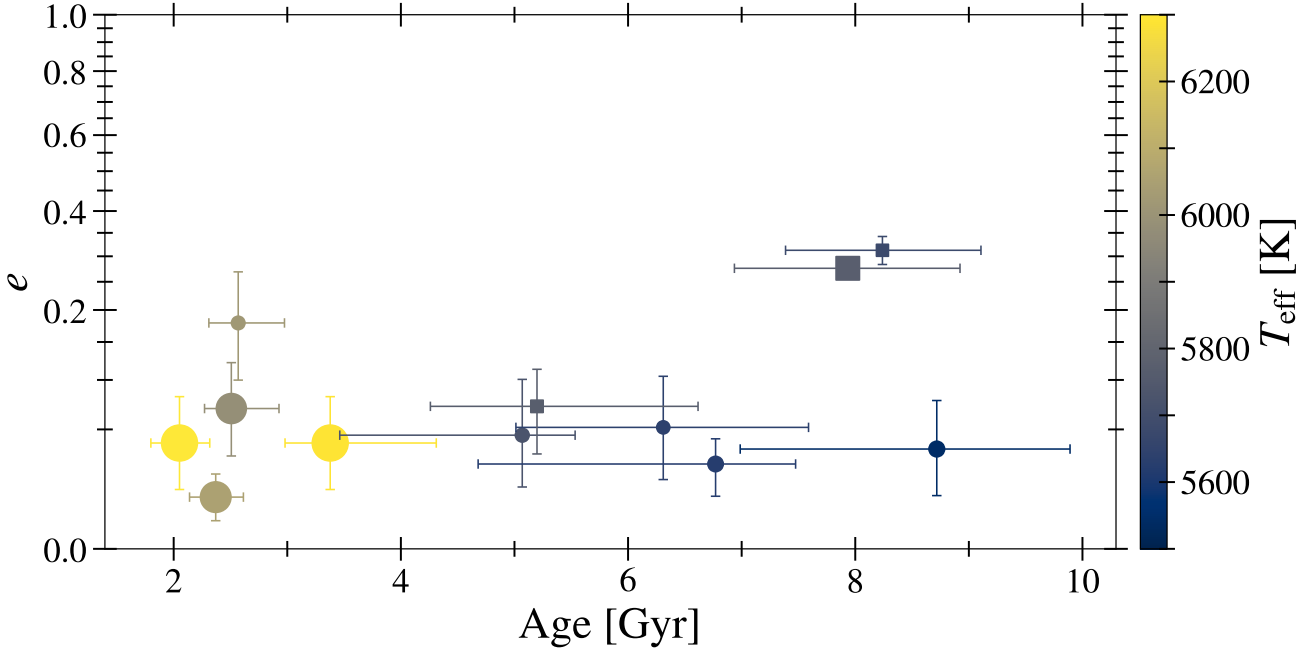


Figure 9. Orbital eccentricity versus age for all hot Jupiters (i.e., $R_p > 8 R_\oplus$ and $P \leq 10$ days) in our sample. The y -axis is scaled non-linearly to emphasize more moderate eccentricities. The effective temperature of the host star is color coded and symbol size scales with planet mass. Planets with non-transiting outer companions are shown as squares.

tion is consistent with the occurrence rate of outer Jovian planets orbiting main-sequence stars.

- The mass-radius diagram for giant planets orbiting subgiant stars roughly matches the observed distribution for main-sequence stars, with the exception of a tentative lack of inflated, massive planets. We also observe that sub-Saturn sized planets orbiting subgiants are systematically more massive than similar sized planets around main-sequence stars, which may be related to detection bias or preferential atmosphere stripping in low-density planets.
- We find tentative evidence for two populations among close-in ($P < 10$ days) giant planets ($R_p > 8 R_\oplus$) orbiting our subgiant sample: 1) “lonely” young (~ 2 Gyr), circular HJs orbiting hot ($T_{\text{eff}} > 6200$ K) stars, and 2) older ($\sim 8 - 10$ Gyr), eccentric ($e \sim 0.3$) HJs orbiting stars with T_{eff} between 5700 – 5900 K where there is evidence for outer companions. Thus the observed properties of hot Jupiters orbiting evolved stars are the likely consequence of multiple formation channels.

Future characterization of planets in this sample will provide a more comprehensive understanding of planet demographics for evolved systems. For example, many of the host stars in this sample are rapidly rotating ($v \sin i > 5$ km s $^{-1}$), facilitating the measurement of projected obliqui-

ties via Rossiter-McLaughlin or Doppler tomography observations (Saunders et al., in prep; Knudstrup et al., in prep). Continued monitoring by TESS and RV surveys will furthermore provide insights into additional planets in these systems.

ACKNOWLEDGEMENTS

The authors wish to recognize and acknowledge the very significant cultural role and reverence that the summit of Maunakea has always had within the Native Hawaiian community. We are most fortunate to have the opportunity to conduct observations from this mountain.

We thank all the observers who spent time collecting data over the many years at Keck/HIRES. We gratefully acknowledge the efforts and dedication of the Keck Observatory staff for support of HIRES and remote observing. We thank the University of California and Google for supporting Lick Observatory and the UCO staff for their dedicated work scheduling and operating the telescopes of Lick Observatory.

A.C. and D.H. acknowledge support from the National Aeronautics and Space Administration (80NSSC21K0652). D.H. also acknowledges support from the Alfred P. Sloan Foundation and the Australian Research Council (FT200100871). N.S. acknowledges support by the National Science Foundation Graduate Research Fellowship Program under Grant Number 2236415. E.K. and S.H.A. acknowledge support from the Danish Council for Independent Research through Grant Number 2032-00230B.

M.L.H. would like to acknowledge NASA support via the FINESST Planetary Science Division, NASA award number 80NSSC21K1536. K.K.M. acknowledges support from the New York Community Trust Fund for Astrophysical Research). E.P. acknowledges financial support from the Agencia Estatal de Investigación of the Ministerio de Ciencia e Innovación MCIN/AEI/10.13039/501100011033 and the ERDF “A way of making Europe” through project PID2021-125627OB-C32, and from the Centre of Excellence “Severo Ochoa” award to the Instituto de Astrofísica de Canarias....

This paper made use of data collected by the TESS mission and are publicly available from the Mikulski Archive for Space Telescopes operated by the Space Telescope Science Institute. Funding for the TESS mission is provided by NASA’s Science Mission Directorate. We acknowledge the use of public TESS data from pipelines at the TESS Science Office and at the TESS Science Processing Operations Center. Resources supporting this work were provided by the NASA High-End Computing Program through the NASA Advanced Supercomputing Division at Ames Research Center for the production of the SPOC data products. This re-

search has made use of the Exoplanet Follow-up Observation Program website, which is operated by the California Institute of Technology, under contract with the National Aeronautics and Space Administration under the Exoplanet Exploration Program. This work has made use of observations (programme IDs: A42/TAC22 and A43/TAC11) from the Italian Telescopio Nazionale Galileo, which is operated on the island of La Palma by the Fundación Galileo Galilei of the Istituto Nazionale di Astrofisica at the Spanish Observatorio del Roque de los Muchachos of the Instituto de Astrofísica de Canarias.

Facilities: APF, Hale (PHARO), HARPS, Keck:I (HIRES), Keck:II (NIRC2), MAST, TESS

Software: We made use of the following publicly-available Python modules: astroquery, emcee (Foreman-Mackey et al. 2013), ktransit, evolstate (Huber et al. 2017; Berger et al. 2018), pySYD (Chontos et al. 2021a,b) and tesspoint.

REFERENCES

- Addison, B. C., Wright, D. J., Nicholson, B. A., et al. 2021, MNRAS, 502, 3704
- Akana Murphy, J. M., Batalha, N. M., Scarsdale, N., et al. 2023, AJ, 166, 153
- Barclay, T., Endl, M., Huber, D., et al. 2015, ApJ, 800, 46
- Batalha, N. E., Lewis, T., Fortney, J. J., et al. 2019, ApJL, 885, L25
- Belokurov, V., Penoyre, Z., Oh, S., et al. 2020, MNRAS, 496, 1922
- Berger, T. A., Huber, D., Gaidos, E., & van Saders, J. L. 2018, ArXiv e-prints, arXiv:1805.00231
- Bowler, B. P., Johnson, J. A., Marcy, G. W., et al. 2010, ApJ, 709, 396
- Burke, C. J., McCullough, P. R., Valenti, J. A., et al. 2008, ApJ, 686, 1331
- Burrows, A., Guillot, T., Hubbard, W. B., et al. 2000, ApJL, 534, L97
- Butler, R. P., Marcy, G. W., Williams, E., et al. 1996, PASP, 108, 500
- Chen, D.-C., Xie, J.-W., Zhou, J.-L., et al. 2023, Proceedings of the National Academy of Science, 120, e2304179120
- Chen, J., & Kipping, D. 2017, ApJ, 834, 17
- Choi, J., Dotter, A., Conroy, C., et al. 2016, ApJ, 823, 102
- Chontos, A., Huber, D., Sayeed, M., & Yamsiri, P. 2021a, arXiv e-prints, arXiv:2108.00582
- Chontos, A., Huber, D., Latham, D. W., et al. 2019, AJ, 157, 192
- Chontos, A., Huber, D., Berger, T. A., et al. 2021b, ApJ, 922, 229
- Chontos, A., Murphy, J. M. A., MacDougall, M. G., et al. 2022, AJ, 163, 297
- Chubak, C., Marcy, G., Fischer, D. A., et al. 2012, arXiv e-prints, arXiv:1207.6212
- Claret, A. 2016, VizieR Online Data Catalog, J/A+A/600/A30
- Cosentino, R., Lovis, C., Pepe, F., et al. 2012, in Society of Photo-Optical Instrumentation Engineers (SPIE) Conference Series, Vol. 8446, Ground-based and Airborne Instrumentation for Astronomy IV, ed. I. S. McLean, S. K. Ramsay, & H. Takami, 84461V
- Dawson, R. I., & Johnson, J. A. 2018, ARA&A, 56, 175
- Eastman, J., Gaudi, B. S., & Agol, E. 2013, PASP, 125, 83
- Evans, D. F. 2018, Research Notes of the American Astronomical Society, 2, 20
- Fabrycky, D., & Tremaine, S. 2007, ApJ, 669, 1298
- Fernandes, R. B., Mulders, G. D., Pascucci, I., Mordasini, C., & Emsenhuber, A. 2019, ApJ, 874, 81
- Foreman-Mackey, D., Hogg, D. W., Lang, D., & Goodman, J. 2013, PASP, 125, 306
- Fulton, B. J., Petigura, E. A., Blunt, S., & Sinukoff, E. 2018, PASP, 130, 044504
- Fulton, B. J., Petigura, E. A., Howard, A. W., et al. 2017, AJ, 154, 109
- Fulton, B. J., Rosenthal, L. J., Hirsch, L. A., et al. 2021, ApJS, 255, 14
- Furlan, E., Ciardi, D. R., Everett, M. E., et al. 2017, AJ, 153, 71
- Gaia Collaboration, Prusti, T., de Bruijne, J. H. J., et al. 2016, A&A, 595, A1

- Gaia Collaboration, Brown, A. G. A., Vallenari, A., et al. 2018, *A&A*, 616, A1
 —. 2021, *A&A*, 649, A1
- Gaia Collaboration, Vallenari, A., Brown, A. G. A., et al. 2023, *A&A*, 674, A1
- Grunblatt, S. K., Huber, D., Gaidos, E., et al. 2018, *ApJL*, 861, L5
- Grunblatt, S. K., Saunders, N., Sun, M., et al. 2022, *AJ*, 163, 120
- Grunblatt, S. K., Saunders, N., Chontos, A., et al. 2023, *AJ*, 165, 44
- Guerrero, N. M., Seager, S., Huang, C. X., et al. 2021, arXiv e-prints, arXiv:2103.12538
- Hamer, J. H., & Schlafman, K. C. 2019, *AJ*, 158, 190
- Hon, M., Huber, D., Rui, N. Z., et al. 2023, *Nature*, 618, 917
- Howard, A. W., Johnson, J. A., Marcy, G. W., et al. 2010, *ApJ*, 721, 1467
- Huang, C. X., Vanderburg, A., Pál, A., et al. 2020a, *Research Notes of the American Astronomical Society*, 4, 204
 —. 2020b, *Research Notes of the American Astronomical Society*, 4, 206
- Huber, D., Zinn, J., Bojsen-Hansen, M., et al. 2017, *ApJ*, 844, 102
- Huber, D., Chaplin, W. J., Chontos, A., et al. 2019, *AJ*, 157, 245
- Hut, P. 1981, *A&A*, 99, 126
- Isaacson, H., & Fischer, D. 2010, *ApJ*, 725, 875
- Jenkins, J. M., Twicken, J. D., McCauliff, S., et al. 2016, *Society of Photo-Optical Instrumentation Engineers (SPIE) Conference Series*, Vol. 9913, The TESS science processing operations center, 99133E
- Johnson, J. A., Morton, T. D., & Wright, J. T. 2013, *ApJ*, 763, 53
- Johnson, J. A., Fischer, D. A., Marcy, G. W., et al. 2007, *ApJ*, 665, 785
- Kabáth, P., Chaturvedi, P., MacQueen, P. J., et al. 2022, arXiv e-prints, arXiv:2205.01860
- Kane, S. R. 2023, *ApJ*, 958, 120
- Kipping, D. M. 2013, *MNRAS*, 435, 2152
- Kolbl, R., Marcy, G. W., Isaacson, H., & Howard, A. W. 2015, *AJ*, 149, 18
- Kraft, R. P. 1967, *ApJ*, 150, 551
- Li, J., Tenenbaum, P., Twicken, J. D., et al. 2019, *PASP*, 131, 024506
- Lopez, E. D., & Fortney, J. J. 2016, *ApJ*, 818, 4
- Lovis, C., & Pepe, F. 2007, *A&A*, 468, 1115
- Lubin, J., Robertson, P., Stefansson, G., et al. 2021, *AJ*, 162, 61
- Lundkvist, M. S., Kjeldsen, H., Albrecht, S., et al. 2016, *Nature Communications*, 7, 11201
- Mandel, K., & Agol, E. 2002, *ApJL*, 580, L171
- Miyazaki, S., & Masuda, K. 2023, *AJ*, 166, 209
- Petigura, E. A. 2015, PhD thesis, University of California, Berkeley
- Petigura, E. A., Howard, A. W., Marcy, G. W., et al. 2017a, *AJ*, 154, 107
- Petigura, E. A., Sinukoff, E., Lopez, E. D., et al. 2017b, *AJ*, 153, 142
- Rodriguez, J. E., Quinn, S. N., Zhou, G., et al. 2021, *AJ*, 161, 194
- Rodriguez, J. E., Quinn, S. N., Vanderburg, A., et al. 2023, *MNRAS*, 521, 2765
- Rosenthal, L. J., Fulton, B. J., Hirsch, L. A., et al. 2021, *ApJS*, 255, 8
- Saunders, N., Grunblatt, S. K., Huber, D., et al. 2022, *AJ*, 163, 53
- Schlafman, K. C., & Winn, J. N. 2013, *ApJ*, 772, 143
- Sha, L., Huang, C. X., Shporer, A., et al. 2021, *AJ*, 161, 82
- Skrutskie, M. F., Cutri, R. M., Stiening, R., et al. 2006, *AJ*, 131, 1163
- Smith, J. C., Stumpe, M. C., Van Cleve, J. E., et al. 2012, *PASP*, 124, 1000
- Stassun, K. G., Oelkers, R. J., Paegert, M., et al. 2019, *AJ*, 158, 138
- Stumpe, M. C., Smith, J. C., Catanzarite, J. H., et al. 2014, *PASP*, 126, 100
- Stumpe, M. C., Smith, J. C., Van Cleve, J. E., et al. 2012, *PASP*, 124, 985
- Taylor, J., Claytor, Z. R., Huber, D., & van Saders, J. 2022, *ApJ*, 927, 31
- Twicken, J. D., Catanzarite, J. H., Clarke, B. D., et al. 2018, *PASP*, 130, 064502
- Van Eylen, V., Albrecht, S., Gandolfi, D., et al. 2016, *AJ*, 152, 143
- Van Eylen, V., Dai, F., Mathur, S., et al. 2018, *MNRAS*, 478, 4866
- Vanderburg, A., Rappaport, S. A., Xu, S., et al. 2020, *Nature*, 585, 363
- Villaver, E., & Livio, M. 2009, *ApJL*, 705, L81
- Vissapragada, S., Chontos, A., Greklek-McKeon, M., et al. 2022, *ApJL*, 941, L31
- Vogt, S. S., Allen, S. L., Bigelow, B. C., et al. 1994, in *Society of Photo-Optical Instrumentation Engineers (SPIE) Conference Series*, Vol. 2198, *Society of Photo-Optical Instrumentation Engineers (SPIE) Conference Series*, ed. D. L. Crawford & E. R. Craine, 362
- Weiss, L. M., Marcy, G. W., Rowe, J. F., et al. 2013, *ApJ*, 768, 14
- Wittenmyer, R. A., Clark, J. T., Trifonov, T., et al. 2022, *AJ*, 163, 82
- Wolszczan, A., & Frail, D. A. 1992, *Nature*, 355, 145
- Wolthoff, V., Reffert, S., Quirrenbach, A., et al. 2022, *A&A*, 661, A63
- Yee, S. W., Petigura, E. A., & von Braun, K. 2017, *ApJ*, 836, 77
- Yu, J., Huber, D., Bedding, T. R., & Stello, D. 2018, *MNRAS*, 480, L48
- Zahn, J.-P. 1977, *A&A*, 57, 383
 —. 1989, *A&A*, 220, 112